Challenges and prospects of 3D micro-supercapacitors for powering the internet of things

Christophe Lethien, Jean Le Bideau, Jean Brousse

Challenges and prospects of 3D micro-supercapacitors for powering the Internet of Things

Christophe Lethien*[a,c], Jean Le Bideau [b,c] and Thierry Brousse [b,c]

The fabrication of miniaturized electrochemical energy storage systems is essential for the development of future electronic devices for Internet of Thing applications where connected devices are increasingly deployed in our daily life. On chip micro-supercapacitors are an attractive solution to fulfill the energy requirements of autonomous, smart, maintenance free and miniaturized sensors but they suffer from a limited energy density and poor technological readiness level in spite of high power capabilities and long cycle life. This paper aims at reviewing the current micro-supercapacitor technologies and at defining the guidelines to produce high performance micro-devices with special focuses onto the 3D designs as well as the fabrication of solid state miniaturized devices to solve the packaging issue.

Broader context

The development of high energy density and solid state micro-supercapacitors is one of the greatest technological challenges at the dawn of the Internet of Thing. Smart and miniaturized power sources are key technologies for the development of cutting edge wireless sensors network for transportation, health and industrial monitoring as well as for environmental applications. Combining the electrochemical capacitor knowledge capitalized for large scale applications with the harvesting / scavenging technologies is essential for the fabrication of autonomous and miniaturized sensor nodes. The high power capabilities and long cycle life of micro-supercapacitors are attractive properties to solve the autonomy issue but the energy density has to be significantly improved while the packaging and safety issues have to be solved. This article reports on a critical review of up-to-date micro-supercapacitor technologies and describes the main challenges and prospects to improve the overall performance and the technological readiness level.

1. Introduction – scope of the review

Internet of Things (IoT) is a trendy concept used to describe the exchange of data between portable, smart and connected devices[1,2]. Such electronic devices could be used as sensors or could be controlled remotely across existing network structure, thus creating opportunities for bridging hardware and software applications in order to design efficient, accurate, self-powered and maintenance-free systems with limited human intervention. Energy scavenging / harvesting technologies are widely investigated for IoT devices to produce self-powering systems with the harvesting from thermal, mechanical or solar energy from the environment and the conversion into electricity. Unfortunately, the intermittence and instability of such resources impose the use of energy storage technologies compatible with the desired application. Miniaturized sensor nodes are required within IoT network for health, environmental or industrial monitoring, drug delivery (*in vivo* application), transportation, wearable personal electronics, radio frequency identification systems. However, it is still challenging to drive these small and connected devices from energy point of view. The miniaturization of different type of electrochemical energy storage (EES) technologies is widely investigated since several years in order to produce efficient EES devices. Li-ion micro-batteries[3–5] (MB) and micro-supercapacitors[6–12] (MSC) are two complementary EES miniaturized systems and have to be used in the energy storage unit of IoT devices. While MB offer high energy (1 $mWh.cm^{-2}$) and moderate power densities (< 5 $mW.cm^{-2}$), MSC are particularly attractive for high power applications (> 10 $mW.cm^{-2}$) but suffer from a lack of energy density (< 0.1 $mWh.cm^{-2}$). The charge storage processes occurring in MB and MSC are totally different in nature leading to complementary properties. MSC based on capacitive ion adsorption/desorption in carbon porous electrodes[10,13,14] offer optimum cycle life (> 1 000 000 cycles) and high power density: such miniaturized EES are characterized by rectangular shape cyclic voltammograms and linear galvanostatic charge-discharge profiles. Similar features are observed with MSC based on pseudocapacitive materials[8,9,15] where fast redox surface reactions are responsible for the continuous change of oxidation state of the cations in electrode material[16,17]: no phase change is observed in pseudocapacitive material during cycling and the electrochemical signatures are capacitive-like. Redox reactions taking place in MB are similar to those occurring in large scale Li-ion batteries.

The current review aims at focusing on micro-supercapacitors technology. In particular, we discuss about the recent progress and challenges to produce high energy density solid state MSC compatible with microelectronic facilities. The first part of this review is dedicated to the description of the topologies and the adequate metrics used to report the general performance of MSC. This part is concluded with a description of electrode materials suitable for MSC. Then, the reported strategies to produce MSC based on thin or thick film technologies are discussed. As the energy density is thickness-limited, a large part of this review is focused on MSC based on 3D architectures taking into account the fabrication of high specific area MSC with high mass loading and robust 3D scaffold. Finally, this review focuses on the electrolyte and packaging issues for MSC which are considered as one of the main technological barrier to improve the technological readiness level (TRL) of such miniaturized EES.

2. Topologies and performance metrics for micro-supercapacitors

The charge storage process involved in supercapacitors and micro-supercapacitors is similar. It is based on capacitive ion adsorption / desorption in porous or nanometer size carbons.

Alternatively, pseudocapacitive materials store charges via fast and reversible redox reactions providing a capacitive-like electrochemical signature. The energy and power densities reached by a MSC are not only dependent on the material properties but also on the topology or configuration of the device. A supercapacitor is composed of two current collectors, two porous electrodes and a separator soaked with a liquid electrolyte. Micro-supercapacitors are considered as a class of miniaturized supercapacitors having a footprint close to several square millimeters. During the last decade, micro-supercapacitors exhibiting high energy and power performance have been reported but the metrics used to normalize the performance are not suitable for miniaturized EES despite the publication of several recent papers focusing on this topic[18–20] and defining the guidelines to report the performance of miniaturized EES devices. The performance of supercapacitors are generally reported using gravimetric values of the capacitance, the power and the energy of the devices ($F.g^{-1}$, $W.kg^{-1}$, $Wh.kg^{-1}$). Unfortunately, small size MSC are surface depending devices and the metrics used to compare the energy and power performance should be tailored to microsystems applications where gravimetric values are useless. In this review, capacitance, energy and power densities are reported respectively in $mF.cm^{-2}$, $\mu Wh.cm^{-2}$ and $mW.cm^{-2}$, leading to footprint areal or surface properties which are the main issue when the surface is limited as in smart and connected miniaturized sensors. At this stage it must be noted that capacitance values are only valid whenever a capacitive-like behavior is depicted for an electrode or a device. Unfortunately many confusing papers are now reporting so called *pseudocapacitive behavior* of nickel or cobalt based oxides or hydroxides in the literature which is wrong and misleading. A recent paper describes the difference between these different kinds of behavior[17], and a perspective paper indicates how to use the different metrics[20]. Obviously when a battery-type electrode or device is proposed, only capacity values can be provided (in $C.g^{-1}$, $mC.cm^{-2}$, $mAh.g^{-1}$, or $mAh.cm^{-2}$).

Volumetric normalized performance (per cm^3) are also widely reported for MSC. While this metric is more suitable for miniaturized EES devices than gravimetric normalization, some misunderstanding or overstatement of the performance are reported for very thin film electrodes (nanometer-thick) and the outstanding volumetric value significantly decreases when the thickness of the active material is increased – if the deposition technique allows to deposit thicker layer. In order to clearly compare the performance of MSC, the surface metrics could be normalized to the thickness of the active layer giving rise to $mF.cm^{-2}.\mu m^{-1}$, $mC.cm^{-2}.\mu m^{-1}$, $\mu Wh.cm^{-2}.\mu m^{-1}$ and $mW.cm^{-2}.\mu m^{-1}$. Such metric is widely reported in the field of micro-battery and could be easily transferred to MSC. A specific attention about the amount of active materials vs the non-active one for MSC should be taken into account. While this strong argument is pertinent when thin film technology (thickness of the electrode < 5 µm vs thickness of substrate ~ 500 µm) compatible with microelectronic industry is used for the fabrication of MSC, most of reported MSC is based on thick film technology where the electrodes could be thicker than 200 µm. In that case, the amount of active vs inactive materials is within the same order of magnitude.

Taking into account surface or areal normalized capacitance, the configuration of the MSC severely impacts the performance (**figure 1**). As a matter of fact, the parallel plate configuration (**figure 1B**) is the most efficient topology when the footprint is limited. The cell areal capacitance (C_{MSC}) is half of the surface capacitance of the single electrode if symmetric device is considered ($C_{MSC} = C_{electrode} / 2$) (**figure 1A**).

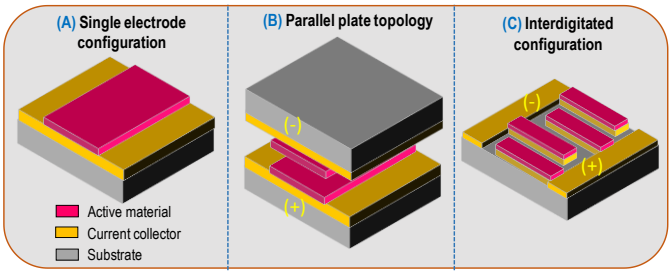

Figure 1 – Overview of the topologies used in the field of micro-supercapacitors

Although this configuration is very attractive from surface point of view, the total volume of the MSC is double since two substrates have to be used to support the two electrodes deposition on current collectors. In between the two plates, a liquid or gel-like electrolyte is used to achieve the MSC fabrication. Due to the thickness of the substrate this stacked design leads to a huge volume which is usually not compatible with MSC applications.

Therefore, as no performing ceramic electrolyte with high ionic conductivity at room temperature is available, only liquid or gel-like electrolyte have to be used. Consequently, the stacked configuration is unusable from a technological point of view as it is impossible to deposit an electrode on a liquid or gel-like electrolyte especially if vacuum deposition technique is used for the electrode preparation. Hence, to reduce the compactness of the MSC while keeping the same footprint area, the two electrodes should be placed in the same plane, i.e. on the same substrate. Interdigitated or interdigital topology is the most suitable configuration for MSC applications. However, the active materials per electrode is reduced (pink color – **figure 1C**) taking into account a reduction by a factor 2 of the active area per electrode and the inactive gap between the two interdigitated electrodes. Consequently, the cell surface capacitance in such topology is less than one fourth of the areal capacitance of a single electrode ($C_{MSC} < C_{electrode} / 4$). Considering the inactive gap between the two interdigitated electrodes is minimized as compared to the total areal of the MSC, we further consider in this review that the $C_{MSC} = C_{electrode} / 4$, in order to compare the performance of MSC (see **tables 1, 2 and 3**). It has nevertheless to be pointed out that the inactive gap is advantageously exploited since it defines the electrolyte localization and thus its thickness. Different shape of the interdigitated electrodes are reported. While the classical pattern (**figure 1C**) is used in 99 % of the reported publications, recent work on spiral-shaped designed interdigitated

electrodes for micro-supercapacitors is published to improve the energy and power densities[21].

It is very important to keep in mind that a MSC is a power miniaturized device able to operate at high cycling rate. Like a supercapacitor, a MSC is characterized by rectangular shape cyclic voltammogram and a time constant $\tau = RC_{MSC}$, where C_{MSC} is the cell capacitance and R the resistance contribution of the device (cell resistance). Consequently, the higher the surface capacitance, the higher the time constant and the lower the power performance: a trade-off should be taken into account between capacitance and power capabilities. Cycle life is another important parameter for a MSC where lifetimes higher than 10 000 cycles should be reported when new results are submitted for publication. Thus capacitance retention upon cycling is a key information. The enhancement of the surface energy density should not be detrimental to the power performance and the cycle life. Self-discharge is another important performance factor which is related to the fading of cell voltage as a function of time, from several hours to several weeks[22,23].

3. Electrode material for MSC

Porous carbon is the main electrode material used in electrochemical capacitors[16] tested in organic electrolytes. Similar trends are observed for carbon based micro-supercapacitors[24–26] and several review papers focusing on carbon electrodes have been published upon the last 5 years[27–30] either for EC or MSC. Carbon electrode with tuned porosity[16] such as activated carbon[31] (AC), onion-like carbon[31] (OLC), carbon nanotubes[32] (CNT), carbide derived carbons[13,25] (CDC) and graphene[33–35] are widely explored for MSC based on ion adsorption / desorption capacitive process. To produce high performance MSC in organic electrolyte, the main issue consists in matching the pore size of the carbon material with the ion size of the electrolyte[36,37]. Among these carbon materials, graphene is well established as a carbon-based electrode. MSC based on Plasma Reduced Graphene (PRG) has been proposed by X. Feng and K. Mullen[38]. Such MSCs have reached an interesting power density (1 $mW.cm^{-2}$) but the energy density is still too low to get autonomous smart miniaturized sensors (1 $nWh.cm^{-2}$). Despite an attractive technology, MSC based on laser-scribed graphene electrodes (LSG) developed by R. Kaner[14,33] clearly suffers from a low areal energy density (0.3 $\mu Wh.cm^{-2}$) while the power density remains interesting (50 $mW.cm^{-2}$). Alternatively, the groups of P. Simon and Y. Gogotsi have developed a carbon-based MSC using either carbon onions (onion-like carbon – OLC) or (AC) activated carbon[10] as the active electrode material. The carbon particles are deposited from a colloidal suspension by electrophoretic deposition technique (EPD) on interdigitated Ti/Au current collectors. While MSCs based on OLC are dedicated to high power applications with outstanding cycling performance at high scan rate (200 $V.s^{-1}$), micro-supercapacitors based on AC exhibit the highest energy density (20 $\mu Wh.cm^{-2}$) reported[10] so far in an organic electrolyte (3 V). The collective fabrication of MSCs based on CDC thin film using Si-compatible microfabrication techniques[13] exhibiting both high areal energy (30 $\mu Wh.cm^{-2}$) and power densities (100 $mW.cm^{-2}$) in organic electrolyte (NEt_4BF_4 in CH_3CN) has been recently reported.

Fast redox reactions occurring at the surface or near surface of pseudocapacitive material in aqueous electrolyte provides higher capacitance than EDLC capacitances in nanoporous carbon electrode.

Pseudocapacitance is used to explain the charge storage mechanism within electrodes where the storage process arises from fast redox reactions with no phase transformation of the electrode material. Pseudocapacitance is faradaic in origin, involving the passage of charge across the double layer, as in battery charging or discharging, but capacitance arises on account of the special relation that can originate for thermodynamic reasons between the extent of charge acceptance (ΔQ) and the change of potential (ΔV), so that a derivative d(ΔQ)/d(ΔV), which is equivalent to a capacitance, can be formulated and experimentally measured by dc, ac, or transient techniques. While this process is basically different from capacitive ion accumulation in porous carbon electrodes, the signature of the pseudocapacitive material is characterized by triangular shape constant current charge/discharge plots and quasi rectangular shape cyclic voltammograms[39]. Consequently, in order to significantly enhance the energy density of MSC, pseudocapacitive materials such as transition or noble metal oxides (RuO_2, MnO_2, Fe_3O_4), nitrides (Mo_xN, TiN, VN, RuN..) or conducting polymers are investigated as efficient electrodes [40–44]. Anhydrous or hydrous ruthenium dioxides (RuO_2) material exhibits a strong pseudocapacitive behaviour (theoretical capacitance > 1300 $F.g^{-1}$) due to the fast redox charge storage process occurring upon protonation of the material when operated in aqueous electrolyte[45,46] combined with its high metallic electrical conductivity (3.10^2 $S.cm^{-1}$). The charge storage process in RuO_2 is described in eq 1.

$$RuO_2 + xH^+ + x.e^- \leftrightarrow RuO_{2-x}(OH)_x \qquad \text{(eq.1) where } 0 < x < 2$$

The continuous change of x during the electro-adsorption of the proton is achieved over more than 1 V electrochemical potential windows leading to high specific capacitance. The hydrous form of RuO_2 ($RuO_2.nH_2O$) exhibits a high gravimetric capacitance (~ 720 $F.g^{-1}$) while the crystalline form of RuO_2 (rutile polymorph) shows lower specific capacitance (350 $F.g^{-1}$). RuO_2 is an expensive material for large scale electrochemical capacitors and other pseudocapacitive materials are investigated as suitable alternative. Nevertheless, for low mass loading electrodes such as observed for MSC, the cost of RuO_2 is limited to several cents of euros, validating the use of this noble metal oxide for miniaturized supercapacitors.

Among all the proposed pseudocapacitive materials, MnO_2 is an earth-abundant, environmentally friendly, low-cost oxide and exhibits high gravimetric capacitance (> 800 $F.g^{-1}$) in neutral aqueous electrolytes despite a low electronic conductivity[40,47,48]. The charge storage mechanism implies at the surface or near surface of the MnO_2 the fast intercalation of protons (H^+) and / or cations ($C^+ = Na^+$, Li^+, K^+…) materials issued from the aqueous electrolyte such as described in eq (2).

$$MnO_2 + xH^+ + yC^+ + (x+y).e^- \leftrightarrow MnOOH_xC_y \quad \text{(eq 2)}$$

where x and y corresponds to the number of moles of H^+ and cations C^+ intercalated in MnO_2.

The last class of pseudocapacitive materials is the transition metal nitride. In 1988, B.E Conway[44] pointed out the pseudocapacitive behaviour of Mo_xN electrode for electrochemical capacitors. Since 2006, vanadium nitride (VN) is investigated[42] as a promising material for supercapacitors based on the multiple oxidation states of the vanadium cation. High capacitance close to 1340 $F.g^{-1}$ in KOH (1 M) at 2 $mV.s^{-1}$ was reported[42] for nanosized VO_xN_y based electrode.

$$VN_xO_y + OH^- \leftrightarrow VN_xO_y \| OH^- + VN_xO_y\text{-}OH \quad \text{(eq 3)}$$

The charge storage mechanism, described in eq (3), arises from the combination of double layer capacitance with pseudocapacitance. Hydroxyl ion (OH^-) is involved in the formation of the electrical double layer as well as in the fast faradic redox reaction occurring on the surface of the partially oxidized vanadium nitride. VN exhibits a high electrical conductivity (12 000 $S.cm^{-1}$), which is a key property for supercapacitor electrodes. In addition, the nanometer-thick vanadium oxide layer is responsible for the high specific pseudocapacitance. Other transition metal nitride materials (TiN, NbN, WN, RuN) have been investigated[49–52] upon the last ten years as efficient pseudocapacitive electrodes for electrochemical capacitors or MSC.

Several type of conducting polymers such as polypyrrole, polyaniline, polythiophene are investigated as pseudocapacitive electrode materials in electrochemical capacitors and MSC[53]. Despite high gravimetric and volumetric capacitances, conducting polymer clearly suffers from a limited stability upon cycling, thus reducing the global performance.

Most of aqueous based electrochemical MSC are built from symmetric electrodes, that is to say that the same material is used in the negative and positive electrodes: RuO_2 / RuO_2 or MnO_2 / MnO_2 MSCs are classically reported leading to the fabrication of symmetric aqueous MSC. In that case, the cell voltage ΔV is limited by the width of the safe electrochemical window of the electrode material in aqueous electrolyte and each electrode of the full device is cycled taking into account ΔV/2 operating potential. To further enhance the energy density of aqueous based MSC, an obvious way is to increase the cell voltage ΔV generally limited to 0.8 V and 1 V for MnO_2 / MnO_2 and RuO_2 / RuO_2 based MSCs respectively. Asymmetric configuration is an attractive solution to fulfill this requirement. By exploiting the gas evolution overpotential, nanoporous carbon / MnO_2 asymmetric MSC[32] have been fabricated following the configuration of classical electrochemical asymmetric supercapacitors[54,55]. Such MSC exhibits up to 2 V cell voltage. The widening of cell voltage ΔV allows to significantly improve the performance (more than four times increase of the energy density). To enhance the energy performance of the LSG technology, R. Kaner has proposed[9] to fabricate asymmetric LSG / MnO_2 MSC. Although the energy density is significantly increased up to 40 $\mu Wh.cm^{-2}$, the 15 µm-thick MnO_2 layer induces some power penalties as routinely observed with transition metal oxides electrodes[9,12].

4. Strategies to enhance the energy density

4.1. From thin to thick film technologies

The aim of this review is to describe the strategies to improve the energy density of MSC without sacrificing the power capabilities as well as the cycle life while keeping constant the footprint area of the miniaturized device. The areal energy density is directly proportional to the surface capacitance value and the square of the cell voltage. While the enhancement of the capacitance is achieved by increasing the thickness of the active material, the improvement of the cell voltage is mainly linked to the used electrolyte (see last section). The notion of "thin film" technology is research community dependent (physics, chemistry, electrical engineering…), that is to say the threshold between thin and thick film is quite ambiguous. Once again, to clearly compare different MSC prototypes, a limitation is fixed in this review: 5 µm-thick layer represents the threshold between what we call the thin and the thick technologies (**figure 2A-B**).

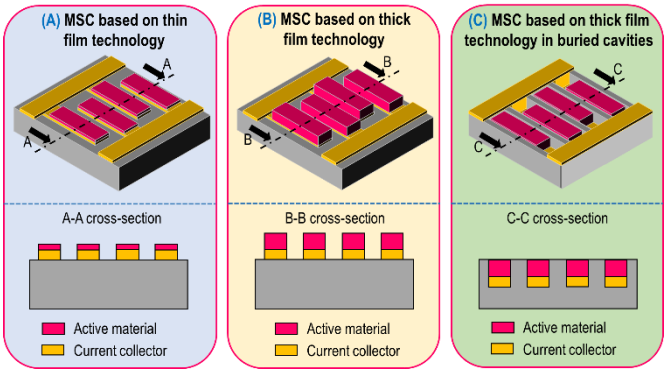

Figure 2 – Comparison between thin (A) and thick (B) film technologies for MSC. Only the film thickness is increased to move from the 1st to the 2nd class of technology. C. Illustration of the thick film technology where the MSC is buried inside a cavity.

Despite the electron and ion transport limitations resulting in the reduction of the power density, thick technology will be described in this review not only to present the high areal capacitance value obtained with this technology but also to highlight a misunderstanding between thick film based MSC buried in cavity and 3D MSC.

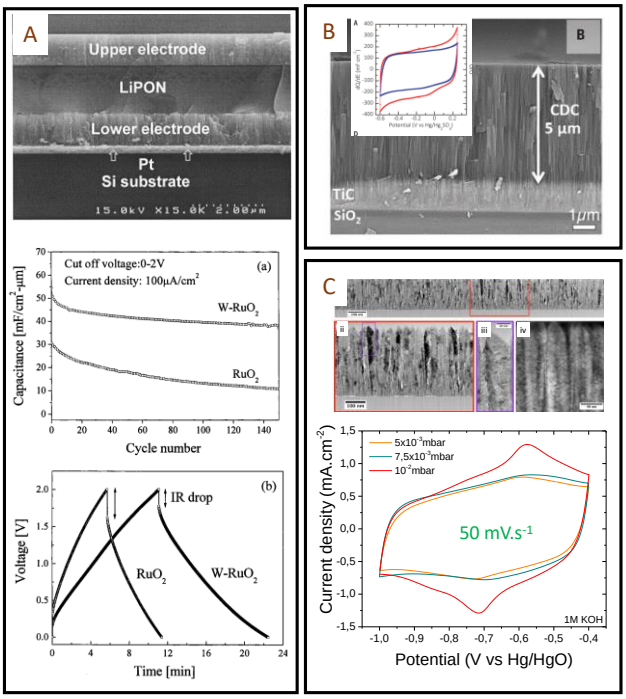

Figure 3 – Overview of thin films based MSC. **A.** Pt / W-RuO_2 / LIPON / W-RuO_2 / Pt stacked layers deposited by sputtering on a silicon wafer[56,57] (W-RuO_2 = tungsten RuO_2): Scanning Electron Microscope cross section imaging, Capacitance retention and Galvanostatic cycling charge / discharge profile. **B.** TiC-CDC electrode[13] produced by a two-step process (inset: cyclic voltamogramm of the electrode in 1 M H_2SO_4 at 1 and 20 $mV.s^{-1}$). **C.** Cross-section analysis (TEM imaging) of sputtered nanoporous vanadium nitride thin films[58]. Such imaging at the nanoscale clearly shows the inter and intra-columnar porosities within the VN sputtered thin film. The cyclic voltamogramms are depicted in 1 M KOH aqueous electrolyte as a function of the deposition pressure to clearly highlight the tuning of the porosity regarding the process parameters.

As a matter of fact, numerous papers have been published since the last 5 years where the authors have claimed the fabrication of 3D micro-supercapacitors whereas deep cavities have been etched in a substrate (**figure 2C**) and filled with a large amount of electrode material to produce high mass loading electrode. In that case, the topology is similar to the thick film technology: the only difference relies upon the burying of the electrode material in substrate cavities. In no way the energy density of such MSC is improved by a 3D effect but rather by thicker layer electrodes buried into cavities.

Intuitively, thin film based MSC (**figure 2A**) will provide lower capacitive performance than thick film technology (**figure 2B**). Nevertheless, the thin film technology (**table 1**) is very attractive due to the easiness of material synthesis / deposition, the fabrication methods (lithography and patterning) and the full device integration widely developed in the semiconductor industry allowing a rapid upscaling of the technological process. Sputtering technique is a deposition process largely developed for thin films in microelectronic (metal, alloys) as well as in the field of micro-battery for the deposition of electrodes, electrolyte and packaging layers[59–64]. The thickness of the layers typically varies from several nanometres up to 5 µm. Sputtering technique was used as pioneered work on MSC in 2001 by Y.S. Yoon *et al* to prepare MSC based on stacked layers[56,57,65] inspired from what is widely developed for micro-battery applications at the beginning of the 2000s. In that case, a solid electrolyte (LIPON) is sandwiched between two RuO_2 (or tungsten-RuO_2, i.e. W-RuO_2) electrodes in contact with two Pt current collectors (**figure 3A**). While the capacitive properties are really interesting for MSC applications (areal capacitance value close to 100 $mF.cm^{-2}$), the low ionic conductivity of the LIPON[66,67] limits the rate capability of miniaturized EES devices due to high ohmic drop. The electrolyte issue – already pointed out in 2001 – is the main technological barrier restraining the technological transfer of the micro-supercapacitors technology from lab scale to pilot production line.

In 2013, TiC-CDC electrodes (1.6 µm-thick) issued from the chlorination process[24] of sputtered titanium carbide thin films are used for the first time as an electrode of interdigitated MSC but the reported capacitance value is too low (6 $mF.cm^{-2}$) to fulfil the energy requirements of IoT applications. Due to a fine optimization between the sputtering and the chlorination processes of metal carbide layers, TiC-CDC electrodes (5 µm-thick) exhibiting an areal capacitance close to 200 $mF.cm^{-2}$ is reported[6,68] in aqueous electrolyte. In that case, the fabrication of nanoporous electrodes is achieved using a two-step process. Until recently, the production of nanoporous electrodes for MSC by sputtering was not investigated despite the publication of porous columnar electrodes[69] for solid oxide fuel cell by pulsed laser deposition technique which is a similar physical deposition tools than sputtering. It is well known that the film morphology of sputtered layer could be tuned regarding the deposition parameters[70,71], following the Thornton structure zone model. Recently, inspired from the previous work[41,42], we have investigated the fine tuning of the porosity of sputtered vanadium nitride (VN) acting as an efficient current collector and pseudocapacitive electrode for micro-supercapacitor applications[58] (**figure 3B**). Inter- and intra-columnar porosities are finely tuned to reach the best trade-off between high electrical conductivity and high surface capacitance value. High performance symmetric VN / VN interdigitated micro-supercapacitors with different mass loadings are fabricated using easy scalable fabrication technique and successfully tested in aqueous electrolyte. An areal capacitance close to 220 $mF.cm^{-2}$ (3.4 µm-thick) is reported for the sputtered VN electrode (optimized porosity), which is in 2018 the best reported value for MSC based on thin film technology (**table 1**). Sputtering technique could also be used to deposit thicker layer (20 µm) at the expense of high deposition time (growth rate ~ 1 $µm.h^{-1}$): in that case, the reached performance are out of scope of this part and will be discussed later when thick film technology will be described.

Variety of methods such as layer by layer[72,73] (LbL) for deposition of carbon nanotubes (CNT) or Mn_3O_4, electrodeposition or the spray coating of Mxene[11] (Ti_3C_2) or multiwall[74] CNT are investigated to produce efficient micro-supercapacitors but the surface capacitance reached by the MSC based on these fabrication methods stays lower than 30 $mF.cm^{-2}$ (see **table 1**). The combination of two deposition techniques to synthesize the electrodes is described in recent

papers. Sputtering and electrodeposition techniques are combined to produce MnO_2 / gold composite thin film electrode (1.6 µm-thick) integrated in a symmetric MSC[75] while asymmetric activated carbon / MnO_2 MSC[32] is proposed based on inkjet printing and electrodeposition techniques (**figure 4**).

To significantly enhance the surface energy density of MSC, one strategy consists in producing thicker electrodes (**table 2**). In that case, deposition techniques used to fabricate miniaturized devices are derived from powder based technology. The main difficulty resides in preventing short circuit between the two electrodes during the deposition process mainly due to the small interspacing distance of the interdigitated configuration (> 5 µm) and the low resolution of the powder based fabrication methods. Solution deposition method[76–79] is widely developed in the field of MSC. Generally, carbon based powder is dispersed in a solvent to form a viscous paste or a diluted suspension depending on the formulation (use of binder, conductive agent…). The suspension or the paste is used to fill deep cavities[80] of the miniaturized interdigitated topology (**figure 5A**): in that case, despite the presence of deep cavities, no 3D effect is highlighted from this topology based only on thick electrodes. To reach this goal, screen printing is a suitable deposition method[80]. With this remark, this review aims at pointing out a misunderstanding in the field of MSC. Electrophoretic deposition from a colloidal suspension[31] is another attractive solution to deposit thick layer (5 up to 7 µm-thick) of carbon particles such as activated carbon (AC) or onion like carbon (OLC). Recently, a high energy density asymmetric MSC (74 µWh.cm^{-2}) based on 3D inkjet printing was reported[81]: as a matter of fact, the printing method is used not only to deposit vanadium based electrodes (400 µm-thick) but also the PVA / LiCl electrolyte (**figure 5B**).

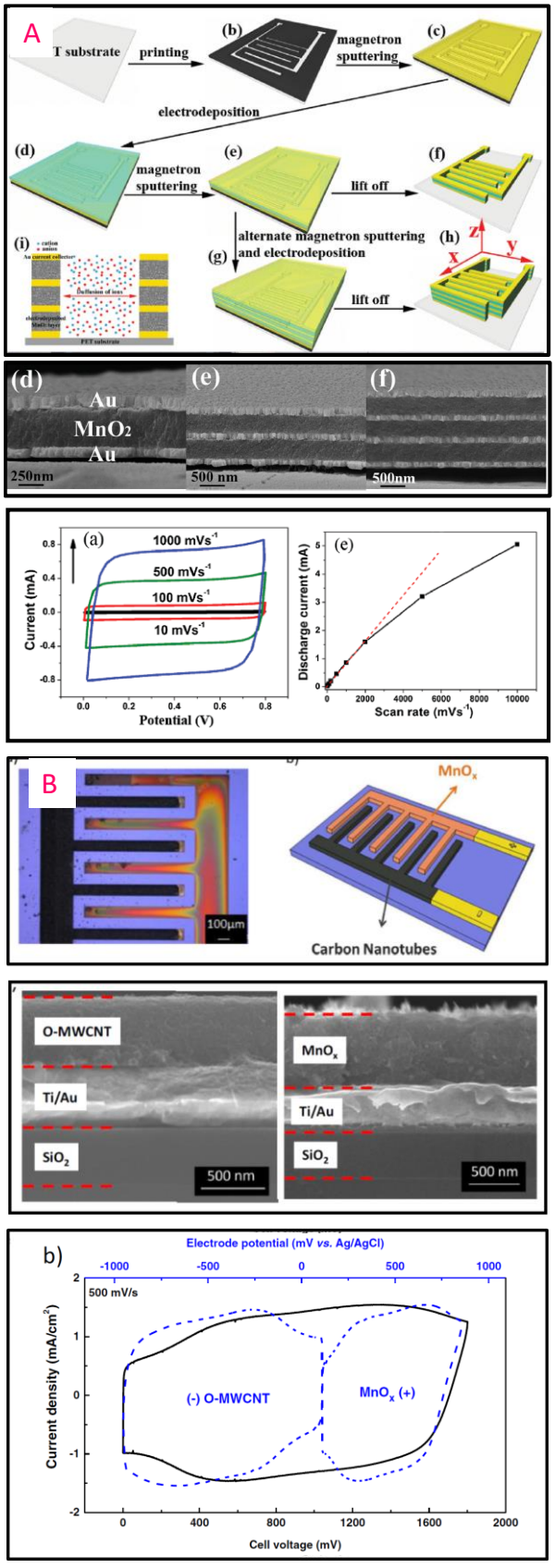

Figure 4 – A. MSC based on thin films technology combining electrodepositon, sputtering to fabricate multilayers composite electrodes and symmetric MSC[75]. **B.** Electrodeposited MnO_2 and inkjet printing of activated carbon are deposited on interdigitated Ti/Au current collectors to produce asymmetric MSC[32].

The mass loading of the printed electrodes is evaluated close to 3 mg.cm^{-2}, i.e. at the same order of magnitude of bulky electrodes. Such mass loading limits the power performance of the asymmetric MSC (< 4 mW.cm^{-2}).

Despite attractive energy density reached by the thick film based MSC configuration, the main limitation deals with the rate capabilities of the thick electrode if material showing low electronic conductivity is used as the active layer without the help of electronically conducting agents. The interspacing resolution is another important issue which limits the technological transfer of the technology from the lab prototyping to large scale deployment.

An attractive way to significantly improve the energy densities of MSCs when the footprint area is limited as in miniaturized devices is to improve the surface to volume ratio.

Thin film deposition on 3D scaffold[3,82–85] leads to the fabrication of high specific area electrode with enhanced capacitance properties while keeping high the rate capability of the electrode due to the restricted thickness of the thin film electrodes. When the active layer is step-conformally deposited on a 3D scaffold exhibiting high area enhancement factor (AEF), the areal capacitance of the 3D MSC is significantly improved at least by one order of magnitude compared to the planar geometry. To fabricate very efficient 3D scaffold, top down and / or bottom up techniques compatible with semiconductor-based processing have to be used. For each approach, the area enhancement factor (i.e. the projected area per footprint area) could be as high as 100, meaning that 1 mm^2 footprint leads to 100 mm^2 projected area. By combining top down and bottom up techniques to fabricate high performance 3D scaffold, an AEF higher than 1000 could be obtained. To demonstrate the potentialities of the 3D technology, some assumptions are considered. A symmetric planar interdigitated MnO_2 / MnO_2 MSC (400 nm-thick, 40 mF.cm^{-2} per electrode, cell voltage = 0.9 V) exhibits an energy density close to 1 µWh.cm^{-2}. If the same thickness of MnO_2 is deposited on 3D interdigitated scaffold exhibiting an AEF close to 1000, the energy density is improved by three order of magnitude to reach 1 mWh.cm^{-2}. Such value is similar to the energy density reached by commercially available micro-batteries[86]. Comparatively, the best areal energy densities[8,9,12,13] reached by 3D MSC are in the range 0.03 to 0.1 mWh.cm^{-2}.

4.2. Micro-supercapacitors with 3D architectures

As previously mentioned, the main bottleneck of MSCs deals with the limited energy density stored in the miniaturized EES to power sensors for IoT applications. The 3D concept of electrochemical energy storage systems is studied since more than 15 years for micro-batteries[4,5,82,87–90] where the main challenges consists in the fabrication of 3D Li-ion all solid state micro-battery. Despite many research efforts, the challenge is quite high due (i) to the difficulty to fabricate efficient 3D architectures with high area enhancement factor and (ii) to the conformal deposition of active material on the 3D template. Planar and 3D micro-batteries are built from a stacked configuration where each layer of the micro-device is deposited on the top of each other, from the current collector to the first electrode (positive or negative one), the solid electrolyte, the second electrode, its current collector and the packing layer.

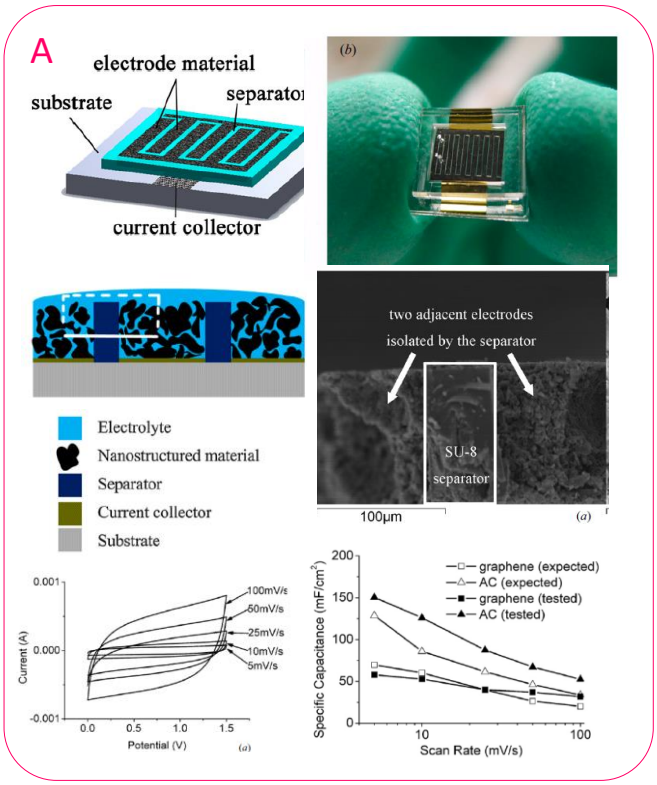

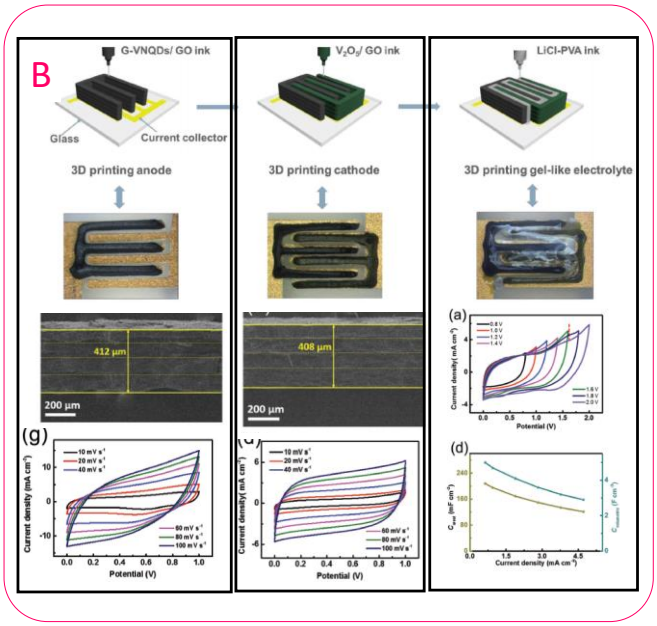

Figure 5 – MSC based on thick films technology. **A.** Carbon electrodes deposited by solution injection technique within SU8 cavity. **B.** Graphene / Vanadium Nitride quantum dots and V_2O_5 / graphene oxide electrodes deposited on interdigitated current collectors by inkjet printing. The gel electrolyte (PVA / LiCl) of the asymmetric MSC is also deposited by this printing method.

Due to the electrolyte issue for MSC (solid electrolyte with high ionic conductivity), the stacked configuration is not a suitable solution not only for planar MSC (as explained in the first part of this review) but

also for a 3D point of view. 3D MSC exhibiting a parallel plate topology[12] is an alternative solution despite the poor integration from microelectronic point of view where parallel or series connection of several MSC (elementary cell) using collective fabrication technique is not possible. In the same way than for thin and thick film configurations, only interdigitated topologies with 3D functionality exhibit the advantages of system integration (miniaturization), and the easiness of parallel and series connection, although the energy density is half the one reached by the parallel plate configuration. The development of specific area with 3D template is widely studied: depending on the dimensions of the 3D scaffold, nano or micro-structured architectures (**figure 6**) are investigated for MSC applications, each of them with their advantages and drawbacks. From a process point of view, nano-architectured or micro-structured interdigitated current collectors **(figure 6A and 6C)** are firstly fabricated based on bottom up synthesis (nanoscale template) or top down approaches (micrometer scale scaffold). Once the 3D interdigitated template is fabricated, the active material is deposited on the scaffold to achieve symmetric or asymmetric 3D MSCs **(figure 6B and 6D)**. Nevertheless, while the fabrication of 3D MSC is interesting from energy density point of view, it should be noted that the use of 3D scaffold may increase the electrical resistance of the 3D MSC. Indeed, taking into account interdigitated electrodes, the ionic pathway between two interpenetrated fingers is higher for planar electrodes than the one for 3D electrodes. Consequently, the areal electrical resistance of the 3D MSC should be increased compared to 2D electrode design.

A large variety of nanostructured templates such as nanowires, nanorods, nano/meso porous template, nanosheets/nanowalls is investigated for MSC applications. Since a significant increase of the energy performance is expected, this AEF should reach a higher value (typically, more than 50, meaning that 1 mm^2 footprint area MSC develops an effective surface close to 50 mm^2). Such an AEF makes nanostructured 3D templating really interesting, but suffers from either a lack of space between two nanostructures (nanowires) to achieve the conformal deposition of significant amount of active material, or from a lack of robustness. This last point is a main drawback that severely hinders the technological transfer toward pilot production line. The lack of space previously pointed out is also meaningful for porous ordered template when the quantity of deposited material is limited by the pore size diameter.

Subsequently, micro-structured vertically aligned 3D scaffold is an attractive solution from robustness point of view. Moreover, the geometrical parameters could be finely tuned to allow the deposition of electrode materials exhibiting a significant thickness (0.5 to 1 µm per electrode) while keeping high the AEF at the same level of magnitude than the 3D nano-architectured scaffold. The design of 3D MSC is a finely tuned trade-off between specific area, material thickness, robustness and targeted technological readiness level.

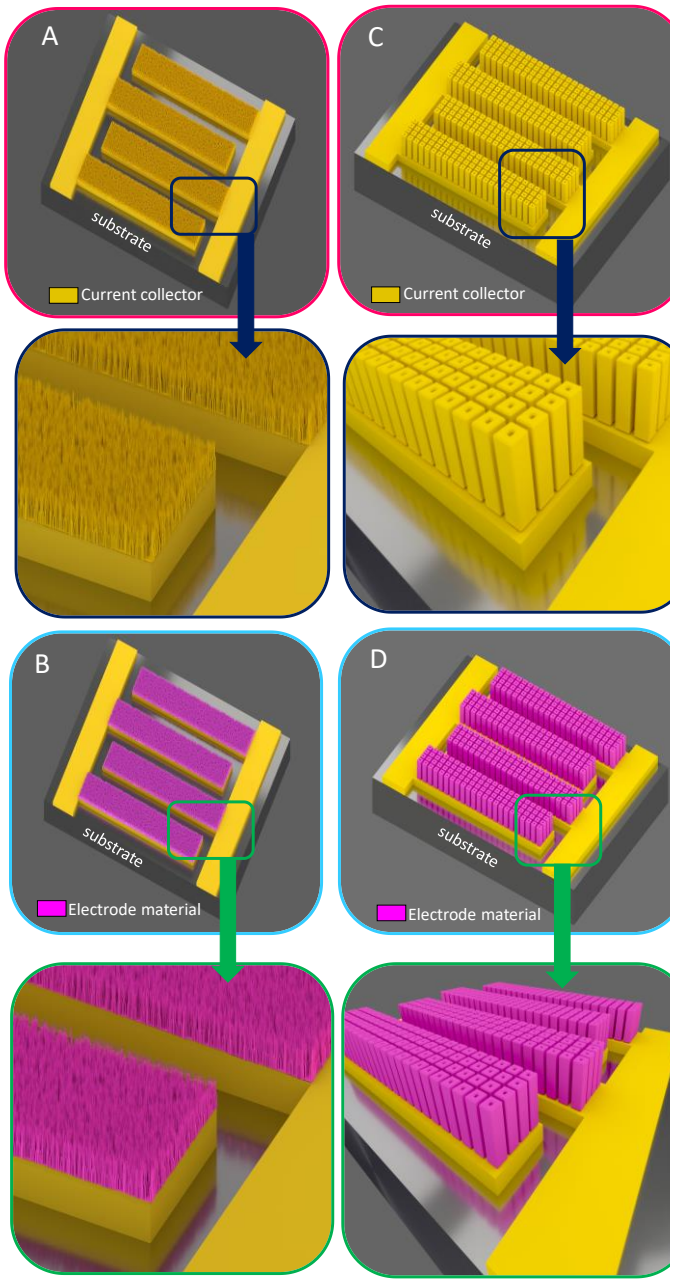

Figure 6 – Overview of the 3D architectures used to enhance the energy density of MSC: from nano to micro-structured scaffold. **A.** The nano-architectured current collector of MSCs based on interdigitated topologies is coated with the active material (pink layers, **B**). In that case, the amount of active material is thickness limited due to the low spacing between two nanostructures (typically less than 50 nm) whereas the specific area of this nanoscale technology is high. **C.** Micro-structured current collector in interdigitated 3D MSC configuration based on micro-tubes technology[8]. **D.** Active material deposited on the 3D micro-tubes current collector. In this configuration, the thickness of electrode material is higher than the nanoscale technology (larger spacing between two microstructures) and the fabricated 3D electrodes are robust from technological point of view.

To optimize the performance of the 3D based EES miniaturized devices, it is crucial to predict the AEF of the 3D scaffold. The diameters of the 3D structures and the spacing between two structures should be tuned to fulfill these requirements. Taking into account straight 3D template and, from mathematical point of view, the AEF of a tubular topology is given by eq (4):

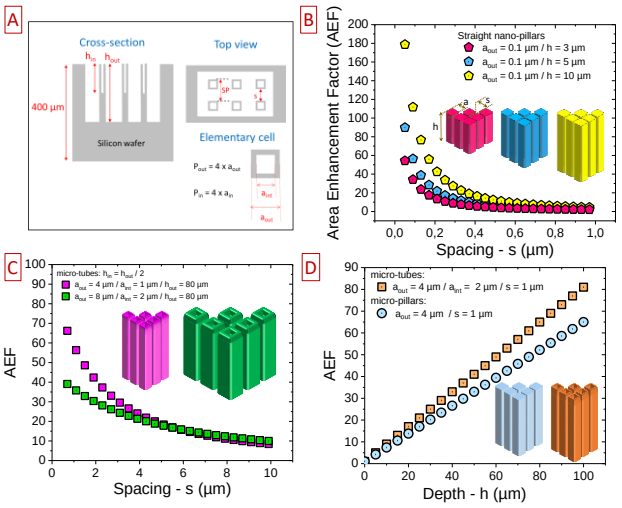

Figure 7 – Numerical modelling of the area enhancement factor (AEF) as a function of the geometrical parameters of the 3D scaffold. **A.** Overview of the 3D scaffold parameters and shape (top view and cross-section). **B.** Evolution of the AEF vs the spacing parameter for nanometre-scale template exhibiting 3 different depths (1, 5 and 10 µm). Not surprisingly, the deeper the scaffold, the higher the AEF. **C.** AEF vs the spacing parameter for 2 micro-tubes scaffold exhibiting double dimension. **D.** Area gain as a function of the depth of the scaffold for micro-pillars and micro-tubes topologies.

$$AEF = \frac{S_{3D}}{S_{2D}} = 1 + \frac{(p_{out} \times h_{out}) + (p_{in} \times h_{in})}{SP^2} \qquad \text{(eq 4)}$$

where *SP* is the structure pitch (the sum of the outer diameter (a_{out}) of a structure and the spacing (s) between two structures), p_{out}, p_{in}, h_{out} and h_{in} are respectively the outer and inner perimeters, the outer and inner depth of the structures. The inner diameter is referred to a_{in} in the **figure 7.** For a pillar based topology, $a_{in} = p_{in} = h_{in} = 0$. The evolution of the AEF depending the selected scaffold is described in **figure 7**.

The geometrical parameters of a micro-tubes topology (square shape) is reported in **figure 7A**. During the fabrication process of the silicon microtubes, the etched rate of the outer surface is twice faster than the inner surface justifying the shape of the cross-section presented in **figure 7A**. As it is reported in **figure 7B**, the spacing between two structures as well as the depth of the structure are key parameters to maximize the AEF.

Regarding nanopillars (nanowires or nanorods – diameter = 100 nm), the deeper the template, the higher the AEF. Moreover, reducing the spacing between two nanopillars improve the density of template, i.e. the number of pillars per square centimetre. Consequently, the AEF is maximized close to 180 for compact and deep 3D nanosized scaffold. At the nanoscale, flexibility is a technological barrier limiting the depth / height of the template. Nevertheless, a compromise has to be found between maximizing the AEF and keeping enough spacing between two nanostructures to allow the deposition of the electrode material. This rationale could be easily translated to micro-sized scaffold as shown in **figure 7C** where the plots exhibit similar shape regarding the spacing parameter. When the dimension of the elementary microstructure is double, the AEF performance is significantly reduced at low spacing (below 4 µm – green plot).

Figure 7D clearly shows the superior performance of microtubes topology as compared to micropillars when regarding similar dimensions. The deeper the microstructures, the better is the AEF. The areal capacitance and so, the surface energy density of MSC are exacerbated owing to the AEF of the 3D scaffold.

However, in order to really observe a 3D enhancement of the surface capacitance, the deposited electrode material should not completely fill the specific surface of the template due to a non-suitable deposition technique. Once the 3D scaffold is finely designed, a key issue deals with the conformal deposition of the electrode material layer on this template. To reach this goal, few deposition methods have to be selected (**table 3**). Chemical vapor deposition of carbon layer (2 nm-thick) has been achieved on silicon nanowires[26] (120 µm-depth). The surface capacitance is close to 325 mF.cm^{-2} owing to the deep nanostructured template whereas the layer thickness is very low due to the reduced spacing between the flexible nanowires. Among the variety of deposition techniques, electrodeposition is one of the best method to achieve the conformal deposition of electrode material layers onto 3D scaffold. This deposition method is used not only for pseudocapacitive metal oxide materials[8,9,12,43,84,91–93] such as MnO_2 and RuO_2 but also for the deposition of conductive polymers[43,94–96] such as polyaniline (PANI) and polypyrrole (PPy). 3D Interdigitated MSC[8,84] based on silicon microtubes or micropillars scaffold are successfully fabricated at the wafer level using a collective fabrication process with areal energy density close to 15 µWh.cm^{-2} while keeping high the power performance (> 10 mW.cm^{-2}). Based on this technology, the reported electrode capacitance varies between 0.5 and 0.7 F.cm^{-2}, depending the geometrical parameters of the scaffold and the thickness of the electrodeposited MnO_2 layer (less than 500 nm-thick). Laser scribed graphene (LSG) is a suitable conductive scaffold for 3D MSC. Based on the published results[33,97,98] on symmetrical planar LSG / LSG or LSG / RuO_2 interdigitated MSCs, R. Kaner and co-workers have focused[9] on the design of asymmetric LSG / MnO_2 MSC. Based on 15 µm-depth LSG scaffold coated with 1 µm-thick MnO_2 thin film, the as-fabricated asymmetric MSC delivers an areal energy density close to 40 µWh.cm^{-2} while the power performance is restricted due to the low electronic conductivity of the 1 µm-thick MnO_2 layer.

In 2015, a high energy density 3D MSC in parallel plate configuration is published[12] by A. Ferris *et al*. showing for the RuO_2 electrode a capacitance of 3.4 F.cm^{-2}, thanks to the combination of macroporous gold scaffold (80 µm-depth) and deposition of thick RuO_2 layers by electrodeposition method. This original approach leads to high areal capacitance electrode but the rate capability of the electrode is affected by the thickness of the RuO_2 layers, limiting the sweep rate (up to 20 mV.s^{-1}) and the time duration (15 minutes) of the charge / discharge cycle.

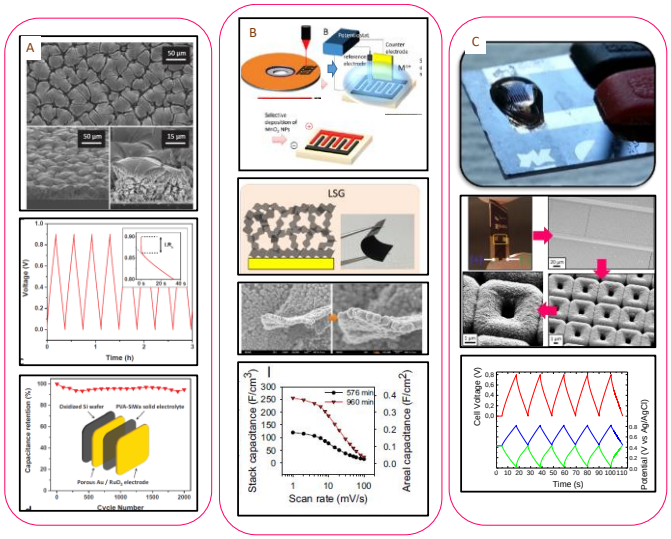

Figure 8 – Overview of lab scale prototype of 3D MSC. **A.** RuO_2 electrodeposited on macroporous gold template in parallel plate configuration. **B.** Laser scribe graphene (LSG) – MnO_2 based asymmetric MSC. **C.** 3D MSC based on the silicon micro-tubes technology and step-conformal electrodeposited MnO_2 on the 3D scaffold.

Another deposition method suitable to achieve the conformal deposition of thin film on complex 3D micro or nanoarchitectured scaffold is the atomic layer deposition technique (ALD). ALD is a powerful technology to deposit thin, pinhole-free and conformal layers on complex substrate[99]. Moreover, nowadays, ALD is available from industrial point of view to deposit thin films on large surfaces (especially in the photovoltaic industry where solar panels with a surface close to 2 m^2 are produced[100]), demonstrating a potential technology transfer compatible with CMOS microelectronic facilities. ALD is a gas phase deposition process based on self-limiting reactions between a volatile precursor and active sites on the surface, enabling a control of the thickness at the atomic level. ALD is widely investigated as a suitable technique for micro-battery applications or the surface modification of powder electrode for large scale battery application[3,5,101–103]. Since several layers can be successively deposited by this technique, ALD is investigated to develop electrode materials for supercapacitors[104–108]: TiN, VO_x and RuO_2 are the most developed electrodes material deposited by ALD for MSC. An attractive solution to reach outstanding areal energy density while keeping the rate capability of a MSC high deals with the fabrication of hierarchical electrode combining several advantages: (i) the robustness and the AEF of the 3D micro-structured template acting as the trunk of the micro-tree, (ii) the AEF of the nano-structured scaffold serving as the branch, taking into account a limited length of the nanostructures, (iii) the deposition of thin film electrode (typically, less than 100 nm) to produce efficient template for the development of high energy and high power MSC.

4.3. Prospect in the design of high performance MSC: towards the fabrication of hierarchical electrode

The hierarchical electrode for MSC concept is reported in **figure 9.** This concept is inspired from the work performed[109] by R. Ghodssi on hierarchical electrodes for micro-battery applications. The conductive hierarchical and interdigitated scaffold consists in several interpenetrated fingers decorated with an array of micro-trees combining both the area gain of a 3D micro-structured and nano-architectured scaffolds **(figure 9A-C)**.

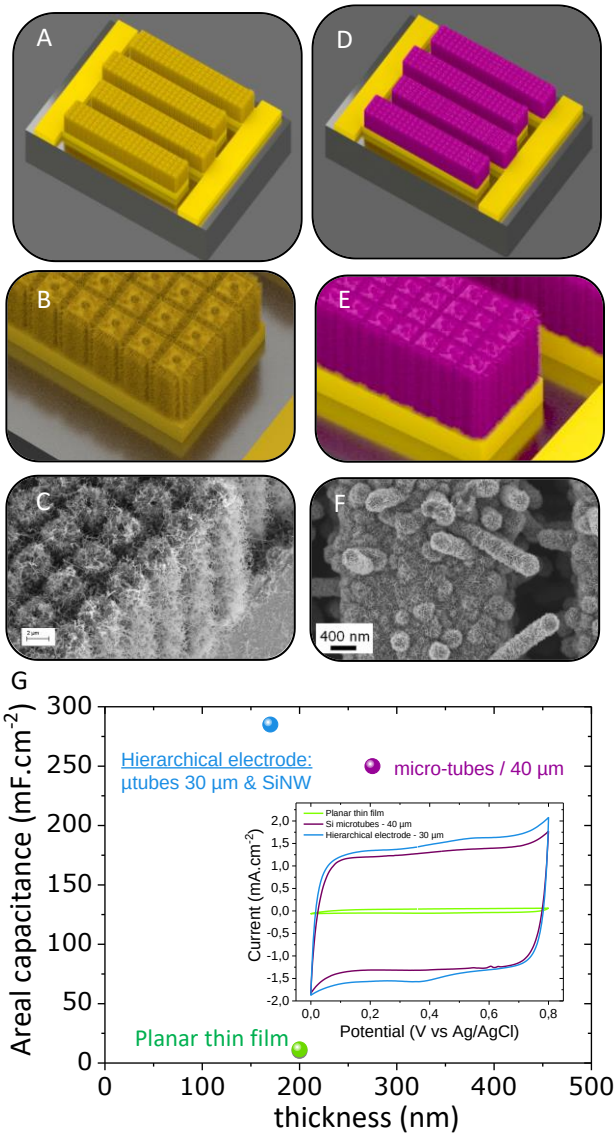

Figure 9 – 3D MSC based on hierarchical electrodes combining top down micro-structured scaffold decorated with bottom up nanoscale structures. **A-B.** 3D interdigitated current collector. **C.** Hierarchical scaffold based on Si micro-tubes and silicon nanowires **D-E.** MSC based on the hierarchical topology and interdigitated configuration. **F.** Hierarchical MnO_2 electrode. **G.** Electrochemical analysis in 0.5 M Na_2SO_4 at 20 $mV.s^{-1}$.

The electrode material layer is then deposited on this hierarchical template (**figure 9D-F**). Following this concept, 3D silicon micro-tubes array fabricated using a top down approach have been decorated with silicon nanowires synthesized by a bottom up vapor liquid solid process (**figure 9E**). 30 nm-thick Pt layer is deposited by ALD on the silicon hierarchical scaffold to provide electronic conductivity to the 3D template. MnO_2 thin film (175 nm-thick) is then electrodeposited by pulsed

potentiostatic technique on the hierarchical micro-trees template. Electrochemical characterization is reported in **figure 9G** in 0.5 M Na_2SO_4 at 20 $mV.s^{-1}$: a comparison is achieved between planar, straight 3D silicon micro-tubes and hierarchical electrodes as a function of the film thickness. The material mass loading is significantly increased by the 3D structures. This is the first conclusion of this work when the 3 CVs are compared. Consequently, the areal capacitance of the 300 nm-thick MnO_2 layer on 40-µm depth Si micro-tubes reaches 250 $mF.cm^{-2}$ at 20 $mV.s^{-1}$. Further improvement of the areal capacitance is observed when the 30 µm- depth micro-tubes array is decorated with silicon nanowires coated with 175 nm-thick MnO_2 layer. In this case, the measured capacitance is close to 300 $mF.cm^{-2}$, i.e. 20% higher than the one measured on straight deeper micro-tubes, thus demonstrating the pertinence of this strategy for MSC.

5 Electrolyte for micro-supercapacitors

Several features are determining good electrolytes: for the sake of high energy storage, at first should come ionic conductivity and the electrochemical window. Water based electrolytes will be limited to ~ 1.2 V (depending on the nature of the electrodes), while organic based electrolytes could allow ~ 2.8 V and ionic liquid (IL) based electrolytes may reach ~ 4 V. The operating temperature range needed will also be a key parameter for selecting an electrolyte since temperature will have effect on ionic conductivity and viscosity, may induce degradation and vaporization. Moreover, a decrease of the temperature may induce liquid-to-solid state or glass phases transitions. This last parameter refers mostly to the physical state of the electrolyte: it is highly desirable to have solid electrolytes in order to limit the packaging and, most often, safety issues.

5.1. Aqueous & organic solvents, and salts

Aqueous electrolytes have been extensively studied since they are cheap and easy to use, but are rather limited due to rather small electrochemical window, and also due to their possible vaporization and solidification[16,110,111]. Often, aqueous acidic H_2SO_4 or alkali KOH electrolytes are studied and provide at 25 °C ionic conductivities of about ~ 1 or 0.6 $S.cm^{-1}$ for 1M H_2SO_4 and 6M KOH respectively. Such 1M H_2SO_4 electrolytes were shown to provide the highest capacities for EDLC with carbon electrodes[112] (up to 300 $F.g^{-1}$). Moreover, they are also efficient for pseudocapacitive materials, either functionalized carbons or oxides such as MnO_2 or RuO_2, showing capacitance[113] up to 1000 $F.g^{-1}$. Nevertheless, some neutral aqueous solutions, with lithium, sodium, potassium sulphate or cholinium chloride salts, showed slightly enhanced potential windows[114,115], up to ~ 2.2 V.

Organic electrolytes, e.g. based on acetonitrile (ACN) or propylene carbonate (PC) with 1M tetraethylammonium tetrafluoroborate (Et_4N BF_4), are now commonly used in commercialized symmetric carbon based electrochemical capacitors thanks to their electrochemical window at ~2.8 V. [36,116]. Nevertheless, ACN or PC with 1M Et_4N BF_4 present ionic conductivities at room temperature (RT) around 0.06 or 0.01 $S.cm^{-1}$ respectively, which is lower than that of water based electrolytes. Other nitrile based solvents such as mononitrile butyronitrile (BTN), or dinitrile solvents glutaronitrile (GTN) and adiponitrile (AND) are studied since they provide wider electrochemical windows. Often, these last solvent show conductivities lower than that of ACN based, although BTN-based solvent present conductivity[117] at RT around 0.02 $S.cm^{-1}$. The salts chosen for the ionic conduction in these organic solvents are also prone to influence the properties of electrolytes. The cation of Et_4N BF_4 salt in PC was shown to be intercalated into graphite, thus limiting the operating cell voltage[118]. Replacement of Pyr14 BF_4 salt allowed to reach cell voltage around 3.2 V, as well as a better capacitance retention thanks to lower ions intercalation in electrodes. This last salt is also a good example of a variable (here, a high amount) amount of dissolved salt in a given solvent, inducing variable effect on viscosity (here, a low effect) and ionic conductivity, either for PC or with ACN[119,120]. It is emphasize that the choice of the salt has to be carried out, besides their electrochemical stability, along with their size as referred of electrode pore size[116,121]. Temperature behaviour may also vary very differently between different solvents; for instance, it was shown, for a given salt (1M Et_4N BF_4), that electrolyte based on PC show more important decreasing resistance and capacitance with decreasing temperature than that with ACN[118]. Moreover, the salt concentration will have effects onto viscosity and conductivity[122] as well as also onto maximum energy, with a threshold effect[123].

One of the main issues regarding organic electrolytes lies in safety due to their flammability and vapour tension. They thus require packaging adequate towards these hazards. However, it is still desirable to increase the electrochemical window above 2.8 V.

5.2. Ionic liquids

Some features of ionic liquids (ILs) answer to these last issues: when chosen adequately, they show very poor flammability and negligible vapour tension[124]. They have attracted much attention since they allow to reach higher voltages, thus higher energy densities, than water and organic solvents. Electrochemical windows up to 3.6 or 4.0 V have been reported[125,126], while increasing operating voltage from 2.7 V (organic solvents) up to 3.7 V would lead to a 50 % energy storage increase[127]. One drawback of ILs is their rather high viscosity and low conductivity, e.g. 0.014 $S.cm^{-1}$ for EMIM BF_4 at RT. Nevertheless, at higher temperatures, where organic solvents and water show non negligible vapour tension, ILs will present lower viscosities and higher conductivities, without safety hazard. They thus present opportunities for devices operating at higher temperatures. Due to trade-off between viscosity, ionic conductivity and electrochemical stability window, most often used ILs for supercapacitors are those based, regarding anions on bis(trifluorosulfonyl)imide (TFSI) or BF_4., and regarding cations pyrrolidinium and imidazolium[128]. Seeing that ILs can often be tailored from a given interesting molecule, redox active electrolytes are being studied and show very good enhancement of the energy[129,130].

5.3. Gels vs Ionogels

Solid electrolytes are the most desirable for many applications, for sake of features such as safety, flexibility, miniaturization. Solid electrolytes are commonly found in the literature as polymer electrolytes or ceramic electrolytes. Ceramic electrolytes for electrochemical capacitors could be either phosphorus-sulphur

based[131] or alumina based[132] ; owing to their quite low conductivities (~1 mS.cm^{-1} at RT), long response time and lack of flexibility,[133] they are not often considered. Although polyelectrolytes are thoroughly studied since they could provide single ion conduction, their application to supercapacitors remains limited due to their relatively low conductivities[134,135] (~ 10^{-5} S.cm^{-1}). Gel polymer electrolytes appear to be the best candidates for all-solid supercapacitors. Gel based on aqueous H_2SO_4 show conductivities as high as that of non-confined aqueous H_2SO_4 electrolyte[133], i.e. ~ 0.7 S.cm^{-1} at RT. Moreover they can present rather low operating temperature[136], down to -10 °C, which could even be improved by the use of 5 mol.kg^{-1} cholinium chloride aqueous solution[115]. Nevertheless, their operating voltage remains limited. Replacement of aqueous acids, e.g. phosphoric acid, by the phosphoric acid ester or cholinium salt leads to an increase of the operating voltage up to 1.3 V or 1.5 V but provide mS.cm^{-1} like conductivities at RT[115,137].

Obtaining gels with ILs thus allows to have wider operating voltage as well as good conductivities. For this purpose, the principal approaches are: (i) to mix pre-formed inorganic particles with ILs to obtain a physical gel; (ii) to swell polymers or inorganic monoliths with ILs; and (iii) to polycondense or polymerize the confining network within these ILs directly, thus obtaining chemical gels[138]. Whereas physical gels are crushable and present lower amounts of ILs, chemical gels, which provide compliant ionogels, confine larger amounts of ILs in order to better preserve and even enhance the dynamics of the liquid state of ILs[139–142]. Such ionogels can be obtained as thin films (10 µm) and flexible membranes, thanks to tuning of the host network features, which can based on a silsesquioxane precursors, a mixture of polymer and siloxane, or a polymer[143,144] (**Figure 10**). Conductivities in the range 1-10 mS.cm^{-1} have been obtained at RT, with operating voltages up to 3.5 V, demonstrated either on 100,000 cycles for MSC[143] or 1200 cycles on lithium micro-batteries. It is here worth to point out that even with these solid-like electrolytes, MSC exhibited time constants almost as short as that of non-confined ILs were obtained, i.e. ~2 and 8 ms for silicon wires and graphene electrodes respectively. Such interesting behavior, which could be surprising for viscous liquids as the studied ILs, appears related to their confinement, and more precisely to the breaking down of interactions between ions in aggregates, present in ILs[140,145].

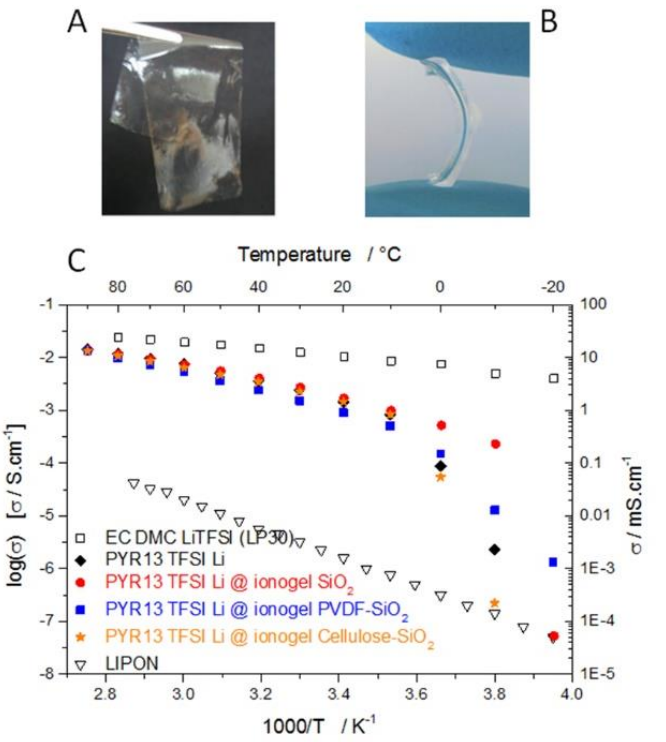

Figure 10 – Ionogel technologies for supercapacitor and MSC. A. 10 µm ionogel films[144]. **B.** Flexible ionogel membranes[143]. **C.** ionic conductivities of carbonate LP30 electrolyte (open squares), LIPON ceramic (open triangles), PYR13 TFSI with Li salt (orange circles) and ionogels obtained by confinement of these electrolyte within different host networks, i.e. mesoporous silica (red circles), hybrid PVDF-silica (blue squares), and cellulose-silica (orange circles).

5.4 Solving the packaging issue to produce solid state micro-supercapacitors

Several routes for shaping ionogels for micro-devices have been presented. When a sol-gel route is used, simple drop casting can be carried out, as shown for micro-supercapacitors[97,146,147] as well as for micro-batteries[138] (**Figure 11**). Further transferable technology can be developed by means of spin coating and ink-jet printing[148,149]. Shaping of polymer based ionogels can also be reached by solution casting or electrospinning after polymer solubilization, with or without a simultaneous sol-gel process[138,150]. Starting from monomers, a fast UV-curing process was also shown to be very efficient[151]. All together these shaping allow an easy packaging of the device, which does not suffer from vapor pressure, and which can moreover sustain few seconds of reflow soldering[143].

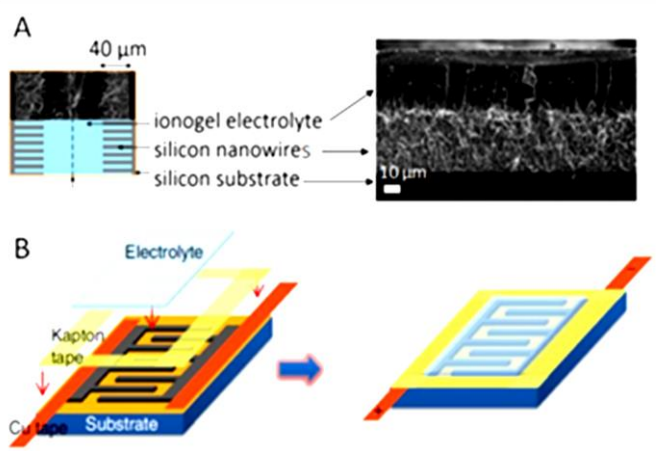

Figure 11 – Integration of ionogel in micro-supercapacitors based on parallel plate of interdigitated topologies. **A.** ionogel obtained after drop casting onto 40 µm long silicon nanowires carpet, assembled face-to-face; the ionogel is formed down to the bottom of the wires and forms simultaneously the solid electrolyte separator[143]. **B.** ionogel casted onto interdigitated electrodes[97].

6 Conclusions and outlooks

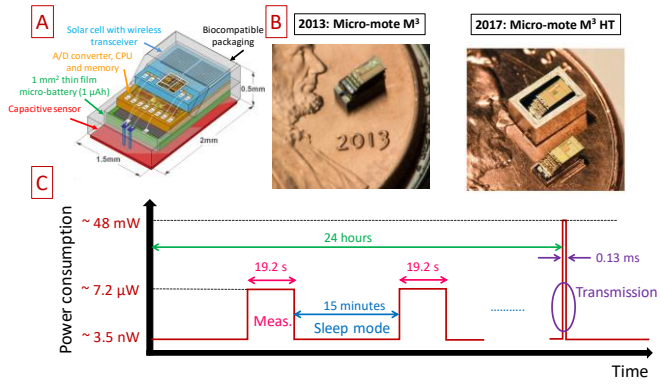

Figure 12 – Overview of the miniaturized sensor nodes for IoT applications. **A.** Schematic of the Michigan Micro Mote[152] (M^3) exhibiting 3 mm2 footprint area. **B.** Images of the M^3 and M^3 HT micro motes[152,153]. **C.** Evolution of the power consumption of the M3 node during 24 hours.

Miniaturized sensor nodes are widely investigated to be implemented within a Wireless Sensor Network (WSN) for the Internet of Things. As mentioned in the present paper, powering these nodes is still challenging due to the miniaturization of such devices[154,155] as well as the surface-limited energy and power densities of available micro-power sources. In practice, the most commonly used power sources to get autonomous such nodes are the primary batteries but it is not an attractive solution to propose maintenance free WSN. To address this last issue, the electrochemical energy storage system should be combined with an energy harvesting system. Commercially of the shelf (COTS) nodes platforms such as IMote 2 from Crossbow[156] or other WSN platforms[157] integrate a primary or a secondary battery, depending to the combination with an energy harvesting system. In that case, the wireless sensor node exhibits a size close to 4.8 x 3.6 cm^2 and more than 10 mW power consumption: the long range application (30 m) is achieved within the Industrial Scientific and Medical (ISM) frequency band using the Zigbee protocol, i.e. at 2.4 GHz, and transmits the data at 250 Kbps. Regarding the size of the devices and the reported power consumption, powering the Imote 2 node with miniaturized electrochemical energy storage such as COTS micro-batteries or MSC prototypes is still difficult despite the integration of ultra-low power electronic devices in the sensor. Recently, significant improvements were made in the fabrication of cubic-millimeter energy-autonomous wireless sensor nodes[152] for health monitoring applications such as intraocular pressure monitoring in the case of Glaucoma disease. The Michigan Micro-Mote M^3 microsystem exhibits 3 mm^2 footprint area and integrates the pressure sensor, the analog to digital conversion and processing unit, a radiofrequency transceiver and an energy unit composed of a thin film micro-battery and a miniaturized solar cell as depicted in the schematic depicted in **figure 12A**. A picture of the M^3 micro-mote and the M^3 HT evolution[153] towards other applications in severe corrosive and high temperature environments is reported in **figure 12B**. The M^3 HT system is an enhancement of the previously reported Michigan Micro Mote (M^3). In that case, such miniaturized and smart sensors fit perfectly with Internet of Things applications. While the integration of 3D MSC and COTS micro-batteries is questionable for powering the Imote 2 sensor exhibiting a large footprint area higher than 17 cm^2, it makes sense to power the M^3 micro-mote (3 mm^2) with such electrochemical energy storage micro-devices. Regarding the evolution of the power consumption as a function of the operating time reported in **figure 12C**, three different phases are identified: the measurement phase, the sleep mode and the transmission phase. The pressure measurements are achieved during 19.2 s every 15 minutes (sleep mode): these two time constants are compatible with the one of micro-batteries. The transmission of the accumulated data is performed daily within the ISM band at 433 or 900 MHz: such wireless data transmission requires a peak power close to 48 mW during 0.13 ms which could not be directly provided by a micro-battery. In ref[152], a 1.6 nF capacitance acts as a local power supply. Nevertheless, the time duration of the data transmission is similar to the time constant of micro-supercapacitors[10,19,33]. While the high areal power density of the MSC technology seems initially attractive, the energy density remains the most critical parameter for IoT nodes thereby limiting the implementation of MSC for many IoT applications. If the areal energy density of the MSC is significantly improved based on the 3D technologies described in this review paper, 3D MSC could be used not only during the transmission but also during the measurement phase. In that case, the 3D MSC acts as a buffer miniaturized power source for the micro-battery which extends its cycle life and the lifetime of the small sensor before needing to be recharged with the harvested solar energy. Moreover, as shown for the M^3 HT micro mote, microdevices operating in harsh conditions (temperature, pressure) are needed[153]. It is thus a challenge to provide miniaturized power sources for designing autonomous smart sensors. However, COTS micro-batteries are not designed to support such harsh conditions. To fulfill the energy requirements in harsh environment, MSC based on ionogel solid electrolyte is an attractive alternative solution to the Cymbet micro-batteries[153]. Along with the design of electrodes with lower footprint, solid electrolytes such as ionogels should answer to this demand since thermally stable host networks are available, and since confined ionic liquids have already been operated at high temperatures, e.g. up to 120 °C for fuel cells[158] or up to 130 °C for waste heat harvesting[127]. Moreover, MSC based on the ionogel technologies[143] have demonstrated the ability to support the reflow soldering process at 250 °C, one of the main important microelectronic process to attach surface mount devices to printed circuit boards.

Emerging IoT applications for health, environmental or industrial monitoring, drug delivery, transportation or wearable personal electronics require integrated and miniaturized electrochemical energy storage systems. To fulfill the energy requirement, micro-supercapacitors technology is widely investigated but up to now there are no MSCs commercially available. While micro-supercapacitors exhibit high power

density and large cycle life, the energy density is limited when footprint area is restricted to several millimeter square. In order to improve the areal energy density of MSCs while keeping constant the footprint area, the current trend is to fabricate 3D micro-supercapacitors with remarkable energy density, i.e. where the areal capacitance of the electrodes is comparable to the one reached by bulky electrodes. Nevertheless, the enhancement of the technological readiness level of such MSC must take into account the collective fabrication of MSC at the wafer level and subsequently process compatibility with MEMS technology instead of lab prototyping. The main technological breakthrough slowing the technological transfer toward pilot production line relies upon the fabrication of solid state MSC. As no standardization is available for reporting the performance of MSC, several key parameters have to be mentioned to compare the submitted results with state of the art values:

- MSC topology: parallel plate or interdigitated.
- Class of MSC: based on thin film, thick film or 3D technology.
- thickness of each layer (µm): substrate, current collectors and electrode. The thickness of the electrolyte could be mentioned if solid state devices is proposed.
- surface (areal) capacitance ($mF.cm^{-2}$) of the electrode and the MSC at different sweep rates or current densities. This value could be normalized regarding the thickness of the electrode ($mF.cm^{-2}.\mu m^{-1}$) to have a better understanding of the intrinsic properties of an electrode and to compare the reached performance of different electrode materials.
- Areal energy and power densities with true performance metrics ($\mu Wh.cm^{-2}$ and $mW.cm^{-2}$). These densities could be normalized regarding the thickness of the electrode to quantify the amount of active material ($\mu Wh.cm^{-2}.\mu m^{-1}$ and $mW.cm^{-2}.\mu m^{-1}$).
- Capacitance retention of the MSC as a function of the number of cycles (cycle life). The sweep rate or the current densities used to measure the MSC performance have to be mentioned and should be in the same order of magnitude than the ones classically used for power devices.

This paper aims at defining the main guidelines and technological roadmap to produce high energy density MSC without sacrificing the power capabilities and taking into account the collective fabrication of the devices at the wafer level. All these arguments plead to implement 3D MSC technology to power IoT devices in the future.

Conflicts of interest

"There are no conflicts to declare".

Acknowledgements

This research is financially supported by the ANR within the DENSSCAPIO project (ANR-17-CE05-0015-02). The authors also want to thank the Ministère de l'Enseignement Supérieur et de la Recherche, Région Hauts de France, FEDER and the French network on electrochemical energy storage (RS2E) for the financial support. The French RENATECH network is greatly acknowledged for the use of microfabrication facilities. The authors want to thank Anne Callewaert for the sketch of the 3D micro-supercapacitors and Djamila Hourlier for the growth of silicon nanowires on 3D micro-structures.

Notes and references

1 A. Whitmore, A. Agarwal and L. Da Xu, *Inf. Syst. Front.*, 2015, 261–274.

2 L. Atzori, A. Iera and G. Morabito, *Comput. Networks*, 2010, **54**, 2787–2805.

3 M. Létiche, E. Eustache, J. Freixas, A. Demortière, V. De Andrade, L. Morgenroth, P. Tilmant, F. Vaurette, D. Troadec, P. Roussel, T. Brousse and C. Lethien, *Adv. Energy Mater.*, 2017, **7**, 1–12.

4 L. Baggetto, R. A. H. Niessen, F. Roozehoom and P. H. L. Notten, *Adv. Funct. Mater.*, 2008, **18**, 1057–1066.

5 C. Liu, E. I. Gillette, X. Chen, A. J. Pearse, A. C. Kozen, M. A. Schroeder, K. E. Gregorczyk, S. B. Lee and G. W. Rubloff, *Nat. Nanotechnol.*, 2014, **9**, 1031–1039.

6 P. Huang, C. Lethien, S. Pinaud, K. Brousse, R. Laloo, V. Turq, M. Respaud, A. Demortière, B. Daffos, P. L. Taberna, B. Chaudret, Y. Gogotsi and P. Simon, *Science (80-.).*, , DOI:10.1126/science.aad3345.

7 M. Létiche, K. Brousse, A. Demortière, P. Huang, B. Daffos, S. Pinaud, M. Respaud, B. Chaudret, P. Roussel, L. Buchaillot, P. L. Taberna, P. Simon and C. Lethien, *Adv. Funct. Mater.*, , DOI:10.1002/adfm.201606813.

8 E. Eustache, C. Douard, A. Demortière, V. De Andrade, M. Brachet, J. Le Bideau, T. Brousse and C. Lethien, *Adv. Mater. Technol.*, 2017, **1700126**, 1700126.

9 M. F. El-Kady, M. Ihns, M. Li, J. Y. Hwang, M. F. Mousavi, L. Chaney, A. T. Lech and R. B. Kaner, *Proc. Natl. Acad. Sci.*, 2015, **112**, 4233–4238.

10 D. Pech, M. Brunet, H. Durou, P. Huang, V. Mochalin, Y. Gogotsi, P.-L. Taberna and P. Simon, *Nat. Nanotechnol.*, 2010, **5**, 651–654.

11 Y.-Y. Peng, B. Akuzum, N. Kurra, M.-Q. Zhao, M. Alhabeb, B. Anasori, E. C. Kumbur, H. N. Alshareef, M.-D. Ger and Y. Gogotsi, *Energy Environ. Sci.*, 2016, **9**, 2847–2854.

12 A. Ferris, S. Garbarino, D. Guay and D. Pech, *Adv. Mater.*, 2015, **27**, 6625–6629.

13 P. Huang, C. Lethien, S. Pinaud, K. Brousse, R. Laloo, V. Turq, M. Respaud, A. Demortiere, B. Daffos, P. L. Taberna, B. Chaudret, Y. Gogotsi and P. Simon, *Science (80-.).*, 2016, **351**, 691–695.

14 M. F. El-Kady and R. B. Kaner, *Nat. Commun.*, 2013, **4**, 1475.

15 E. Eustache, R. Frappier, R. L. Porto, S. Bouhtiyya, J. F. Pierson and T. Brousse, *Electrochem. commun.*, 2013, **28**, 104–106.

16 P. Simon and Y. Gogotsi, *Nat. Mater.*, 2008, **7**, 845–854.

17 T. Brousse, D. Belanger and J. W. Long, *J. Electrochem. Soc.*, 2015, **162**, A5185–A5189.

18 Y. Gogotsi and P. Simon, *Science (80-.).*, 2011, **334**, 917–918.

19 M. Beidaghi and Y. Gogotsi, *Energy Environ. Sci.*, 2014, **7**,

867.
20 A. Balducci, D. Belanger, T. Brousse, J. W. Long and W. Sugimoto, *J. Electrochem. Soc.*, 2017, **164**, A1487–A1488.
21 X. Tian, M. Shi, X. Xu, M. Yan, L. Xu, A. Minhas-Khan, C. Han, L. He and L. Mai, *Adv. Mater.*, 2015, **27**, 7476–7482.
22 T. Liu, W. G. Pell and B. E. Conway, *Electrochim. Acta*, 1997, **42**, 3541–3552.
23 J. Kowal, E. Avaroglu, F. Chamekh, A. Šenfelds, T. Thien, D. Wijaya and D. U. Sauer, *J. Power Sources*, 2011, **196**, 573–579.
24 J. Chmiola, C. Largeot, P. L. Taberna, P. Simon and Y. Gogotsi, *Science (80-.).*, 2010, **328**, 480–483.
25 M. Heon, S. Lofland, J. Applegate, R. Nolte, E. Cortes, J. D. Hettinger, P.-L. Taberna, P. Simon, P. Huang, M. Brunet and Y. Gogotsi, *Energy Environ. Sci.*, 2011, **4**, 135–138.
26 J. P. Alper, S. Wang, F. Rossi, G. Salviati, N. Yiu, C. Carraro and R. Maboudian, *Nano Lett.*, 2014, **14**, 1843–1847.
27 Z. S. Wu, X. Feng and H. M. Cheng, *Natl. Sci. Rev.*, 2014, **1**, 277–292.
28 G. Xiong, C. Meng, R. G. Reifenberger, P. P. Irazoqui and T. S. Fisher, *Electroanalysis*, 2014, **26**, 30–51.
29 W. Gu and G. Yushin, *Wiley Interdiscip. Rev. Energy Environ.*, 2014, **3**, 424–473.
30 C. Xu, B. Xu, Y. Gu, Z. Xiong, J. Sun and X. S. Zhao, *Energy Environ. Sci.*, 2013, **6**, 1388.
31 D. Pech, M. Brunet, H. Durou, P. Huang, V. Mochalin, Y. Gogotsi, P.-L. Taberna and P. Simon, *Nat. Nanotechnol.*, 2010, **5**, 651–654.
32 T. M. Dinh, F. Mesnilgrente, V. Conédéra, N. A. Kyerematen and D. Pech, *J. Electrochem. Soc.*, 2015, **162**, 2016–2020.
33 M. F. El-Kady, V. Strong, S. Dubin and R. B. Kaner, *Science (80-.).*, 2012, **335**, 1326–1330.
34 D. Yu, K. Goh, H. Wang, L. Wei, W. Jiang, Q. Zhang, L. Dai and Y. Chen, *Nat. Nanotechnol.*, 2014, **9**, 555–562.
35 W. Gao, N. Singh, L. Song, Z. Liu, A. L. M. Reddy, L. Ci, R. Vajtai, Q. Zhang, B. Wei and P. M. Ajayan, *Nat. Nanotechnol.*, 2011, **6**, 496–500.
36 C. Largeot, C. Portet, J. Chmiola, P. L. Taberna, Y. Gogotsi and P. Simon, *J. Am. Chem. Soc.*, 2008, **130**, 2730–2731.
37 J. Chmiola, G. Yushin, Y. Gogotsi, C. Portet, P. Simon and P. L. Taberna, *Science (80-.).*, 2006, **313**, 1760–1763.
38 Z. Wu, K. Parvez, X. Feng and K. Müllen, *Nat. Commun.*, 2013, **4**, 2487.
39 B. E. Conway, in *Electrochemical Supercapacitors Scientific Fundamentals and Technological Applications*, 1999, pp. 221–257.
40 M. Toupin, T. Brousse and D. Bélanger, *Chem. Mater.*, 2004, **16**, 3184–3190.
41 R. Lucio-Porto, S. Bouhtiyya, J. F. Pierson, A. Morel, F. Capon, P. Boulet and T. Brousse, *Electrochim. Acta*, 2014, **141**, 203–211.
42 D. Choi, G. E. Blomgren and P. N. Kumta, *Adv. Mater.*, 2006, **18**, 1178–1182.
43 D. P. Dubal, D. Aradilla, G. Bidan, P. Gentile, T. J. S. Schubert, J. Wimberg, S. Sadki and P. Gomez-Romero, *Sci. Rep.*, 2015, **5**, 9771.
44 T.-C. Liu, W. G. Pell, S. L. Roberson and B. E. Conway, *J. Electrochem. Soc.*, 1998, **145**, 1882.
45 G. Lodi, E. Sivieri, A. De Batisti and S. Trasatti, *J. Appl. Electrochem.*, 1978, **8**, 135–143.
46 S. Hadži-Jordanov, H. Angerstein-Kozlowska, M. Vukovic and B. E. Conway, *J. Electrochem. Soc.*, 1978, **125**, 1471.
47 H. Y. Lee and J. B. Goodenough, *J. Solid State Chem.*, 1999, **144**, 220–223.
48 M. Toupin, T. Brousse and D. Belanger, *Chem. Mater.*, 2002, **14**, 3946–3952.
49 A. Achour, R. L. Porto, M.-A. Soussou, M. Islam, M. Boujtita, K. A. Aissa, L. Le Brizoual, A. Djouadi and T. Brousse, *J. Power Sources*, 2015, **300**, 525–532.
50 S. Bouhtiyya, R. Lucio Porto, B. Laïk, P. Boulet, F. Capon, J. P. Pereira-Ramos, T. Brousse and J. F. Pierson, *Scr. Mater.*, 2013, **68**, 659–662.
51 O. Kartachova, A. M. Glushenkov, Y. Chen, H. Zhang and Y. Chen, *J. Mater. Chem. A*, 2013, **1**, 7889.
52 H. Cui, G. Zhu, X. Liu, F. Liu, Y. Xie, C. Yang, T. Lin, H. Gu and F. Huang, *Adv. Sci.*, 2015, **2**, 1–12.
53 G. A. Snook, P. Kao and A. S. Best, *J. Power Sources*, 2011, **196**, 1–12.
54 T. Brousse, M. Toupin and D. Bélanger, *J. Electrochem. Soc.*, 2004, **151**, A614.
55 V. Khomenko, E. Raymundo-Piñero and F. Béguin, *J. Power Sources*, 2006, **153**, 183–190.
56 Y. S. Yoon, W. I. Cho, J. H. Lim and D. J. Choi, *J. Power Sources*, 2001, **101**, 126–129.
57 H.-K. Kim, S.-H. Cho, Y.-W. Ok, T.-Y. Seong and Y. S. Yoon, *J. Vac. Sci. Technol. B Microelectron. Nanom. Struct.*, 2003, **21**, 949.
58 K. Robert, C. Douard, A. Demortière, F. Blanchard, P. Roussel, T. Brousse and C. Lethien, *Adv. Mater. Technol.*, 2018, **1800036**, 1–12.
59 D. W. Murphy, P. A. Christian, F. J. DiSalvo, C. Tsang, A. Dananjay, J. Kim, A. Manthiram, H. I. Schlesinger, H. C. Brown, A. E. Finholt, J. R. Gilbreath, H. R. Hoekstra, E. K. Hyde, J. Amer, X. Yu, J. B. Bates, G. E. Jellison and F. X. Hart, *J. Electrochem. Soc. Sci. This J. Carides, J. V. Waszczak, ibid. Inorg. Chem. Chem. Soc. This J.*, 1997, **144965**, 150–1115.
60 N. Balke, S. Jesse, A. N. Morozovska, E. Eliseev, D. W. Chung, Y. Kim, L. Adamczyk, R. E. García, N. Dudney and S. V. Kalinin, *Nat. Nanotechnol.*, 2010, **5**, 749–754.
61 J. Li, C. Ma, M. Chi, C. Liang and N. J. Dudney, *Adv. Energy Mater.*, 2015, **5**, 1–6.
62 V. P. Phan, B. Pecquenard and F. Le Cras, *Adv. Funct. Mater.*, 2012, **22**, 2580–2584.
63 M. Létiche, M. Hallot, M. Huvé, T. Brousse, P. Roussel and C. Lethien, *Chem. Mater.*, 2017, **29**, 6044–6057.
64 T. Pichonat, C. Lethien, N. Tiercelin, S. Godey, E. Pichonat, P. Roussel, M. Colmont and P. A. Rolland, *Mater. Chem. Phys.*, 2010, **123**, 231–235.
65 J. H. Lim, D. J. Choi, H.-K. Kim, W. Il Cho and Y. S. Yoon, *J. Electrochem. Soc.*, 2001, **148**, A275.
66 J. B. Bates, N. J. Dudney, B. Neudecker, A. Ueda and C. D. Evans, *Solid State Ionics*, 2000, **135**, 33–45.
67 T. Pichonat, C. Lethien, N. Tiercelin, S. Godey, E. Pichonat,

P. Roussel, M. Colmont and P. A. Rolland, *Mater. Chem. Phys.*, 2010, **123**, 231–235.
68 M. Létiche, K. Brousse, A. Demortière, P. Huang, B. Daffos, S. Pinaud, M. Respaud, B. Chaudret, P. Roussel, L. Buchaillot, P. L. Taberna, P. Simon and C. Lethien, *Adv. Funct. Mater.*, 2017, **27**, 1–10.
69 W. Jung, J. O. Dereux, W. C. Chueh, Y. Hao and S. M. Haile, *Energy Environ. Sci.*, 2012, **5**, 8682.
70 J. A. Thornton, *J. Vac. Sci. Technol. A Vacuum, Surfaces, Film.*, 1986, **4**, 3059–3065.
71 J. A. Thornton, *Annu. Rev. Mater. Sci.*, 1977, **7**, 239–260.
72 S. Y. Hong, J. Yoon, S. W. Jin, Y. Lim, S. Lee and G. Zi, *ACS Nano*, 2014, 8844–8855.
73 Y. Lim, J. Yoon, J. Yun, D. Kim, S. Y. Hong, S. J. Lee, G. Zi and J. S. Ha, *ACS Nano*, 2014, **8**, 11639–11650.
74 D. Kim, G. Lee, D. Kim and J. S. Ha, *ACS Appl. Mater. Interfaces*, 2015, **7**, 4608–4615.
75 H. B. Hu, Z. B. Pei, H. J. Fan and C. H. Ye, *Small*, 2016, **12**, 3059–3069.
76 C. Shen, X. Wang, W. Zhang and F. Kang, *J. Power Sources*, 2011, **196**, 10465–10471.
77 J. Pu, X. Wang, T. Zhang, S. Li and J. Liu, *Nanotechnology*, 2016, **27**, 45701.
78 X. Wang, H. Xing, C. Shen and S. Li, *Micro Nano Lett.*, 2012, **7**, 1166–1169.
79 S. Li, X. Wang, H. Xing and C. Shen, *J. Micromechanics Microengineering*, , DOI:10.1088/0960-1317/23/11/114013.
80 H. Durou, D. Pech, D. Colin, P. Simon, P.-L. Taberna and M. Brunet, *Microsyst. Technol.*, 2012, **18**, 467–473.
81 K. Shen, J. Ding and S. Yang, *Adv. Energy Mater.*, 2018, **1800408**, 1800408.
82 J. W. Long, B. Dunn, D. R. Rolison and H. S. White, *Chem. Rev.*, 2004, **104**, 4463–4492.
83 H. S. Min, B. Y. Park, L. Taherabadi, C. Wang, Y. Yeh, R. Zaouk, M. J. Madou and B. Dunn, *J. Power Sources*, 2008, **178**, 795–800.
84 E. Eustache, C. Douard, R. Retoux, C. Lethien and T. Brousse, *Adv. Energy Mater.*, 2015, **5**, 3–7.
85 M. Beidaghi and C. Wang, *Adv. Funct. Mater.*, 2012, **22**, 4501–4510.
86 Cymbet Corporation, *Data Sheet*, 2010, 1–5.
87 E. Eustache, P. Tilmant, L. Morgenroth, P. Roussel, G. Patriarche, D. Troadec, N. Rolland, T. Brousse and C. Lethien, *Adv. Energy Mater.*, 2014, **4**, 1–11.
88 M. Létiche, E. Eustache, J. Freixas, A. Demortière, V. De Andrade, L. Morgenroth, P. Tilmant, F. Vaurette, D. Troadec, P. Roussel, T. Brousse and C. Lethien, *Adv. Energy Mater.*, , DOI:10.1002/aenm.201601402.
89 M. Roberts, P. Johns, J. Owen, D. Brandell, K. Edstrom, G. El Enany, C. Guery, D. Golodnitsky, M. Lacey, C. Lecoeur, H. Mazor, E. Peled, E. Perre, M. M. Shaijumon, P. Simon and P.-L. Taberna, *J. Mater. Chem.*, 2011, **21**, 9876.
90 C. Lethien, M. Zegaoui, P. Roussel, P. Tilmant, N. Rolland and P. A. Rolland, *Microelectron. Eng.*, 2011, **88**, 3172–3177.
91 Y. Q. Li, X. M. Shi, X. Y. Lang, Z. Wen, J. C. Li and Q. Jiang, *Adv. Funct. Mater.*, 2016, **26**, 1830–1839.
92 Z. Su, C. Yang, B. Xie, Z. Lin, Z. Zhang, J. Liu, B. Li, F. Kang and C. P. Wong, *Energy Environ. Sci.*, 2014, **7**, 2652–2659.
93 A. Ponrouch, S. Garbarino, E. Bertin and D. Guay, *J. Power Sources*, 2013, **221**, 228–231.
94 X. Lang, L. Zhang, T. Fujita, Y. Ding and M. Chen, *J. Power Sources*, 2012, **197**, 325–329.
95 M. Beidaghi and C. Wang, *Electrochim. Acta*, 2011, **56**, 9508–9514.
96 J. Maeng, Y. J. Kim, C. Meng and P. P. Irazoqui, *ACS Appl. Mater. Interfaces*, 2016, **8**, 13458–13465.
97 M. F. El-Kady and R. B. Kaner, *Nat. Commun.*, 2013, **4**, 1475.
98 J. Y. Hwang, M. F. El-Kady, Y. Wang, L. Wang, Y. Shao, K. Marsh, J. M. Ko and R. B. Kaner, *Nano Energy*, 2015, **18**, 57–70.
99 S. M. George, *Chem. Rev.*, 2010, **110**, 111–131.
100 J. A. van Delft, D. Garcia-Alonso and W. M. M. Kessels, *Semicond. Sci. Technol.*, 2012, **27**, 074002.
101 J. Liu and X. Sun, *Nanotechnology*, 2015, **26**, 024001.
102 H.-M. Cho, M. V. Chen, A. C. MacRae and Y. S. Meng, *ACS Appl. Mater. Interfaces*, 2015, **7**, 16231–16239.
103 S. Ouendi, C. Arico, F. Blanchard, J. Codron, X. Wallart, P. Louis, P. Roussel, L. Clavier and P. Simon, *Energy Storage Mater.*, 2018, 1–8.
104 E. Kao, C. Yang, R. Warren, A. Kozinda and L. Lin, *Sensors Actuators, A Phys.*, 2016, **240**, 160–166.
105 R. Warren, F. Sammoura, F. Tounsi, M. Sanghadasa and L. Lin, *J. Mater. Chem. A*, 2015, **3**, 15568–15575.
106 K. Grigoras, J. Keskinen, L. Grï¿½nberg, E. Yli-Rantala, S. Laakso, H. Vï¿½limï¿½ki, P. Kauranen, J. Ahopelto and M. Prunnila, *Nano Energy*, 2016, **26**, 340–345.
107 P. Lu, P. Ohlckers, L. Müller, S. Leopold, M. Hoffmann, K. Grigoras, J. Ahopelto, M. Prunnila and X. Chen, *Electrochem. commun.*, 2016, **70**, 51–55.
108 S. Boukhalfa, K. Evanoff and G. Yushin, *Energy Environ. Sci.*, 2012, **5**, 6872–6879.
109 K. Gerasopoulos, E. Pomerantseva, M. McCarthy, A. Brown, C. Wang, J. Culver and R. Ghodssi, *ACS Nano*, 2012, **6**, 6422–6432.
110 X. Zang, R. Zhang, Z. Zhen, W. Lai, C. Yang, F. Kang and H. Zhu, *Nano Energy*, 2017, **40**, 224–232.
111 R. S. Borges, A. L. M. Reddy, M. T. F. Rodrigues, H. Gullapalli, K. Balakrishnan, G. G. Silva and P. M. Ajayan, *Sci. Rep.*, 2013, **3**, 1–6.
112 D. Jiménez-Cordero, F. Heras, M. A. Gilarranz and E. Raymundo-Piñero, *Carbon N. Y.*, 2014, **71**, 127–138.
113 X. Liu and P. G. Pickup, *J. Solid State Electrochem.*, 2010, **14**, 231–240.
114 K. Fic, G. Lota, M. Meller and E. Frackowiak, *Energy Environ. Sci.*, 2012, **5**, 5842–5850.
115 Q. Abbas and F. Béguin, *ChemSusChem*, 2018, **11**, 975–984.
116 J. Chmiola, G. Yushin, Y. Gogotsi, C. Portet and P. L. Taberna, *Science (80-.).*, 2006, **7**, 1760–1764.
117 A. R. Neale, C. Schütter, P. Wilde, P. Goodrich, C. Hardacre, S. Passerini, A. Balducci and J. Jacquemin, *J. Chem. Eng. Data*, 2017, **62**, 376–390.

118 L. J. Hardwick, M. Hahn, P. Ruch, M. Holzapfel, W. Scheifele, H. Buqa, F. Krumeich, P. Novak and R. Kotz, *Electrochim. Acta*, 2006, **52**, 675–680.

119 S. Pohlmann and A. Balducci, *Electrochim. Acta*, 2013, **110**, 221–227.

120 J. Krummacher and S. Passerini, *Chemelectrochem*, 2017, **4**, 353–361.

121 S. Pohlmann, C. R. Castro and A. Balducci, *J. Electrochem. Soc.*, 2015, **162**, A5020–A5030.

122 M. Ue, *Electrochemistry*, 2007, **8**, 565–572.

123 J. Zheng and T. Jow, *J. Electrochem. Soc.*, 1997, **144**, 2417–2420.

124 M. Armand, F. Endres, D. R. MacFarlane, H. Ohno and B. Scrosati, *Nat. Mater.*, 2009, **8**, 621–629.

125 A. Balducci, W. A. Henderson, M. Mastragostino, S. Passerini, P. Simon and F. Soavi, *Electrochim. Acta*, 2005, **50**, 2233–2237.

126 C. Arbizzani, M. Biso, D. Cericola, M. Lazzari, F. Soavi and M. Mastragostino, *J. Power Sources*, 2008, **185**, 1575–1579.

127 D. R. MacFarlane, N. Tachikawa, M. Forsyth, J. M. Pringle, P. C. Howlett, G. D. Elliott, J. H. Davis, M. Watanabe, P. Simon and C. A. Angell, *Energy Environ. Sci.*, 2014, **7**, 232–250.

128 A. Brandt, S. Pohlmann, A. Varzi, A. Balducci and S. Passerini, *MRS Bull.*, 2013, **38**, 554–559.

129 E. Mourad, L. Coustan, P. Lannelongue, D. Zigah, A. Mehdi, A. Vioux, S. A. Freunberger, F. Favier and O. Fontaine, *Nat. Mater.*, 2016, **16**, 446–453.

130 B. Gorska, E. Frąckowiak and F. Béguin, *Curr. Opin. Electrochem.*, , DOI:10.1016/J.COELEC.2018.05.006.

131 B. E. Francisco, C. M. Jones, S.-H. Lee and C. R. Stoldt, *Appl. Phys. Lett.*, 2012, **100**, 103902.

132 A. S. Ulihin, Y. G. Mateyshina and N. F. Uvarov, *Solid State Ionics*, 2013, **251**, 62–65.

133 I. Stepniak and A. Ciszewski, *Electrochim. Acta*, 2011, **56**, 2477–2482.

134 F. N. Ajjan, M. Ambrogi, A. Tiruye, D. Cordella, A. M. Fernandes, K. Grygiel, M. Isik, N. Patil, L. Porcarelli, G. Rocasalbas, E. Zeglio, M. Antonietti, C. Detrembleur, O. Inganäs, C. Jérôme, R. Marcilla, D. Mecerreyes, M. Moreno, D. Taton and J. Yuan, *Polym Int*, 2017, **66**, 1119–1128.

135 G. Rydzek, Q. Ji, M. Li, P. Schaaf, J. P. Hill, F. Boulmedais and K. Ariga, *Nano Today*, 2015, 1–30.

136 S. Yamazaki, A. Takegawa, Y. Kaneko, J. Kadokawa and M. Yamagata, *J. Power Sources*, 2010, **195**, 6245–6249.

137 A. Ł. Anna, I. A. Rutkowska, P. Taberna, P. Simon and P. J. Kulesza, *J. Power Sources*, 2015, **274**, 1147–1154.

138 J. Le Bideau, J. Ducros, P. Soudan and D. Guyomard, *Adv. Funct. Mater.*, 2011, **21**, 4073–4078.

139 N. Butchtova, A. Guyomard-Lack and J. Le Bideau, *Green Chem.*, 2014, **16**, 1149–1152.

140 A. Guyomard-Lack, P.-E. Delannoy, N. Dupré, C. V Cerclier, B. Humbert and J. Le Bideau, *Phys. Chem. Chem. Phys.*, 2014, **16**, 23639–23645.

141 C. Iacob, J. R. Sangoro, W. K. Kipnusu, R. Valiullin, J. Karger and F. Kremer, *Soft Matter*, 2012, **8**, 289–293.

142 A. Guyomard-Lack, B. Said, N. Dupré, A. Galarneau and J. Le Bideau, *New J. Chem.*, 2016, **40**, 4269–4276.

143 M. Brachet, D. Gaboriau, P. Gentile, S. Fantini, G. Bidan, S. Sadki, T. Brousse and J. Le Bideau, *J. Mater. Chem. A*, 2016, **4**, 11835–11843.

144 A. Guyomard-lack, J. Abusleme, P. Soudan, B. Lestriez, D. Guyomard and J. Le Bideau, *Adv. Energy Mater.*, 2014, **4**, 1301570.

145 R. Futamura, T. Iiyama, Y. Takasaki, Y. Gogotsi, M. J. Biggs, M. Salanne, J. Ségalini, P. Simon and K. Kaneko, *Nat. Mater.*, 2017, **16**, 1225–1234.

146 L. Negre, B. Daffos, P. L. Taberna and P. Simon, *J. Electrochem. Soc.*, 2015, **162**, A5037–A5040.

147 M. Brachet, T. Brousse and J. Le Bideau, *ECS Electrochem. Lett.*, 2014, **3**, A112–A115.

148 D. S. Ashby, R. H. Deblock, C. Lai, C. S. Choi and B. S. Dunn, *Joule*, 2017, 1–15.

149 P. E. Delannoy, B. Riou, B. Lestriez, D. Guyomard, T. Brousse and J. Le Bideau, *J. Power Sources*, 2015, **274**, 1085–1090.

150 A. Taubert, *Eur. J. Inorg. Chem.*, 2015, 1148–1159.

151 C. Gerbaldi, J. R. Nair, G. Meligrana, R. Bongiovanni, S. Bodoardo and N. Penazzi, *Electrochim. Acta*, 2010, **55**, 1460–1467.

152 G. Chen, H. Ghaed and R. Haque, *IEEE Int. Solid-State Circuits Conf.*, 2011, 138–139.

153 M. Choi, Y. Sui, I. H. Lee, R. Meredith, Y. Ma, G. Kim, D. Blaauw, Y. B. Gianchandani and T. Li, *Sensors*, 2017, **17**, 2190.

154 D. Steingart, S. Roundy, P. K. Wright and J. W. Evans, *MRS Bull.*, 2008, **33**, 408–409.

155 A. Raj and D. Steingart, *J. Electrochem. Soc.*, 2018, **165**, 3130–3136.

156 Crossbow, *6020-0117-02 Rev A*, 2–4.

157 G. A. Al-suhail, J. Mehdi and G. Nikolakopoulos, *J. Commun. Technol. Electron. Comput. Sci.*, 2017, 23–30.

158 T. Yasuda and M. Watanabe, *MRS Bull.*, 2013, **38**, 560–566.

159 J. H. Sung, S. J. Kim and K. H. Lee, *J. Power Sources*, 2004, **133**, 312–319.

160 W. Si, C. Yan, Y. Chen, S. Oswald, L. Han and O. G. Schmidt, *Energy Environ. Sci.*, 2013, **6**, 3218.

161 Y. S. Yoon, W. I. Cho, J. H. Lim and D. J. Choi, *J. Power Sources*, 2001, **101**, 126–129.

162 J. Xu and G. Shen, *Nano Energy*, 2015, **13**, 131–139.

163 P. Huang, M. Heon, D. Pech, M. Brunet, P. L. Taberna, Y. Gogotsi, S. Lofland, J. D. Hettinger and P. Simon, *J. Power Sources*, 2013, **225**, 240–244.

164 D. Pech, M. Brunet, P. L. Taberna, P. Simon, N. Fabre, F. Mesnilgrente, V. Conédéra and H. Durou, *J. Power Sources*, 2010, **195**, 1266–1269.

165 B. Hsia, J. Marschewski, S. Wang, J. Bin In, C. Carraro, D. Poulikakos, C. P. Grigoropoulos and R. Maboudian, *Nanotechnology*, 2014, **25**, 055401.

166 P. Huang, D. Pech, R. Lin, J. K. McDonough, M. Brunet, P. L. Taberna, Y. Gogotsi and P. Simon, *Electrochem. commun.*, 2013, **36**, 53–56.

167 J. Lin, C. Zhang, Z. Yan, Y. Zhu, Z. Peng, R. H. Hauge, D.

Natelson and J. M. Tour, *Nano Lett.*, 2013, **13**, 72–78.
168 R.-Z. Li, R. Peng, K. D. Kihm, S. Bai, D. Bridges, U. Tumuluri, Z. Wu, T. Zhang, G. Compagnini, Z. Feng and A. Hu, *Energy Environ. Sci.*, 2016, **9**, 1458–1467.
169 K. Brousse, P. Huang, S. Pinaud, M. Respaud, B. Daffos, B. Chaudret, C. Lethien, P. L. Taberna and P. Simon, *J. Power Sources*, 2016, **328**, 520–526.
170 L. Li, J. Zhang, Z. Peng, Y. Li, C. Gao, Y. Ji, R. Ye, N. D. Kim, Q. Zhong, Y. Yang, H. Fei, G. Ruan and J. M. Tour, *Adv. Mater.*, 2016, **28**, 838–845.
171 S. M. Mirvakili and I. W. Hunter, *Adv. Mater.*, 2017, **29**, 1–6.
172 C. Shen, X. Wang, S. Li, J. Wang, W. Zhang and F. Kang, *J. Power Sources*, 2013, **234**, 302–309.
173 C. Meng, J. Maeng, S. W. M. John and P. P. Irazoqui, *Adv. Energy Mater.*, 2014, **4**, 1–7.
174 Z. S. Wu, K. Parvez, S. Li, S. Yang, Z. Liu, S. Liu, X. Feng and K. Mullen, *Adv. Mater.*, 2015, **27**, 4054–4061.
175 C. Shen, X. Wang, W. Zhang and F. Kang, *J. Power Sources*, 2011, **196**, 10465–10471.
176 D. Aradilla, D. Gaboriau, G. Bidan, P. Gentile, M. Boniface, D. Dubal, P. Gómez-Romero, J. Wimberg, T. J. S. Schubert and S. Sadki, *J. Mater. Chem. A*, 2015, **3**, 13978–13985.
177 T. M. Dinh, A. Achour, S. Vizireanu, G. Dinescu, L. Nistor, K. Armstrong, D. Guay and D. Pech, *Nano Energy*, 2014, **10**, 288–294.

Table 1 Electrochemical performance of micro-supercapacitors based on **thin film** topology

Ref	Electrode material[a]		Electrode capacitance*	Areal power density	Device topology	Electrolyte[b] / Cell voltage (V)
	Deposition technique	Thickness (µm)	($mF.cm^{-2}$)	($mW.cm^{-2}$)		
159	Ppy (ED)	2.5	-	-	Interdigitated	0.1 M H_3PO_4
38	Graphene (Plasma rGO)	0.015	0.32	0.75[i]	Interdigitated	PVA H_2SO_4 / 1 V
73	MWCNT (LbL)	0.25	0.32	0.8[i]	Interdigitated	Ionogel (EMIM - TFSI / PEGDA) / 3 V
72	MWCNT / Mn_3O_4 (LbL)	0.22	0.64	0.5[i]	Interdigitated	PVA H_3PO_4 / 0.8 V
74	MWCNT (spray coating)	0.5	1.04	1.05[i]	Interdigitated	Ionogel (EMIM - TFSI / PEGDA) / 2 V
160	MnO_2 - Au stacked layers (e-beam evaporation)	0.05	1.6	0.017[i]	Interdigitated	PVA H_2SO_4 / 0.8 V
161	RuO_2 (sputtering)	0.2	2.8	-	Parallel Plate	LIPON / 2.5 V
162	rGO (solution)	1.2	3.2	0.09[i]	Interdigitated	PVA KOH / 0.8 V
163	TiC-CDC (sputtering)	1.6	6	84[ii]	Interdigitated	1 M NEt_4 - BF_4 in PC
164	AC (IJP)	2	8.4	44.9[ii]	Interdigitated	1 M NEt_4 - BF_4 in PC / 2.5 V
32	MWCNT (IJP) and MnO_2 (ED)	0.5 and 0.6	9.6	675[ii]	Interdigitated	0.5 M Na_2SO_4 / 1.8 V
11	Mxene Ti_3C_2 (spray coating)	1.3	27	1.95[i]	Interdigitated	PVA H_2SO_4 / 0.6 V
65	RuO_2 (sputtering)	0.3	45.6	-	Parallel Plate	LIPON / 2 V
75	MnO_2 - Au stacked layers (ED and sputtering)	1.6	48	-	Interdigitated	1 M Na_2SO_4 / 0.8 V
13	TiC-CDC (sputtering)	4.1	69	100[i]	Parallel Plate	2 M EMIM - BF_4 in AN / 3 V
57	W-RuO_2 (sputtering)	1	100	-	Parallel Plate	LIPON / 2 V
7	TiC-CDC (sputtering)	3.2	103	100[i]	Single electrode	1 M H_2SO_4 / 0.9 V
13	TiC-CDC (sputtering)	5	205	-	Interdigitated	1 M H_2SO_4 / 0.9 V
58	VN (sputtering)	3.4	220	10[i]	Interdigitated	1 M KOH / 0.6 V

[a] AC = Activated Carbon, rGO = reduced graphene oxide, MWCNT = multiwall carbon nanotubes, CDC = carbide derived carbon, PPy = Polypyrrole, LbL = layer by layer, ED = electrodeposition, IJP = inkjet printing, * If not mention, estimated from $C_{electrode} = 4 \times C_{MSC}$ for interdigitated topology and $C_{electrode} = 2 \times C_{MSC}$ for parallel plate configuration, [b] EMIM = 1-ethyl-3-methylimidazolium, TFSI = bis(trifluoromethanesulfonyl)imide, NEt_4 = tetraethylammonium, BF_4 = tetrafluoroborate, PEGDA = poly(ethylene glycol) diacrylate, PVA = poly(vinyl alcohol), PC = propylene carbonate, AN = acetonitrile, [i] = max of the instantaneous power, [ii] = maximum power

Table 2 Electrochemical performance of micro-supercapacitors based on thick film topology

Ref	Electrode material[a]		Electrode capacitance*	Areal power density	Device topology	Electrolyte[b] / Cell voltage (V)
	Deposition technique	Thickness (µm)	($mF.cm^{-2}$)	($mW.cm^{-2}$)		
165	VA CNT (CVD)	50	1.2	100[i]	Interdigitated	Ionogel (EMIM - TFSI / TMOS) / 3 V
35	rGO electrode (GO filtration and DLW)	22	2	220[i]	Parallel plate	1M Na_2SO_4 / 1 V
166	OLC (EPD)	7	4.4	240[ii]	Interdigitated	PIP_{13}-FSI - PYR_{14}-FSI Ionic Liquid / 3.7 V
85	rGO - CNT electrode (ESD)	6	5	46.2[i]	Interdigitated	3 M KCl / 1V
31	OLC (EPD)	7	6.8	210[i]	Interdigitated	1 M NEt_4 - BF_4 in PC / 3V
14	Graphene (LSG)	7.6	7.1	152[i]	Interdigitated	Ionogel (BMIM – TFSI / Fused Silica) / 2.5 V
167	Graphene – CNT electrode (CVD)	20	8	60[i] - 230[ii]	Interdigitated	1 M Na_2SO_4 / 1 V
14	Graphene (LSG)	7.6	9.1	53[i]	Interdigitated	PVA H_2SO_4 / 1 V
31	AC (EPD)	5	18	20[i]	Interdigitated	1 M NEt_4 - BF_4 in PC / 3V
168	rGO - Au composite electrode (solution and DLW)	13.7	20	-	Interdigitated	PVA H_2SO_4 / 1 V
169	TiC-CDC (sputtering)	7	72	5.3[i]	single electrode	2M EMIM - BF_4 in ACN / 3 V
170	Graphene- FeOOH / Graphene-MnO_2 electrodes (LIG combined with ED)	41	88	11.8[i]	Interdigitated	PVA LiCL / 1.8 V
171	Vertically Aligned Nb nanowires (BDP)	1 000	100	1000[i]	Parallel plate	1 M H_2SO_4 / 1 V
172	AC and MnO_2 (IDP)	10	120	7[i]	Interdigitated	0.2 M K_2SO_4 / 1.5 V
98	Graphene / RuO_2 (LSG)	7.6	160	6[i]	Interdigitated	1 M H_2SO_4 / 1 V
173	PANI nanowires (ED)	10.1	180	10.1[i]	-	PVA H_2SO_4 / 0.9 V
80	AC (Screen printing)	215	324	34.4[i]	Interdigitated	1M NEt_4 - BF_4 in PC / 2.5 V
174	Graphene - PANI staked electrode (LbL)	4.5	326	4.5[i]	Interdigitated	PVA H_2SO_4 / 1 V
175	AC (solution injection)	70	360	51.5[i]	Interdigitated	1 M $NaNO_3$ / 1 V
77	AC (solution injection)	250	536	4.5[i]	Interdigitated	PVA H_3PO_4 / 1 V
78	AC (solution injection)	100	640	31.2[i]	Interdigitated	BMIM - BF_4 Ionic Liquid
81	V_2O_5 and G-VNQD electrodes (3D printing)	100	832	3.77[i]	Interdigitated	PVA LiCL / 1.6 V
79	AC (solution injection)	200	1244	10[i]	Interdigitated	BMIM - BF_4 Ionic Liquid / 3 V

[a] LSG = Laser-scribed Graphene, CVD = chemical vapour deposition, ESD = Electrostatic spray deposition, DLW = Direct Laser Writing, BDP = bundle drawing procedure, OLC = Onion Like Carbon , EPD = electrophoretic deposition, ED = electrodeposition, IDP= injecting drying process, LIG = laser induced graphene, AC = Activated Carbon, rGO = reduced graphene oxide, CNT = carbon nanotubes, VA CNT = Vertically Aligned CNT, CDC = carbide derived carbon, PANI = polyaniline, G-VNQD = graphene and vanadium nitride quantum dots, * If not mention, estimated from $C_{electrode} = 4 \times C_{MSC}$ for interdigitated topology and $C_{electrode} = 2 \times C_{MSC}$ for parallel plate configuration, [b] BMIM = 1-butyl-3-methylimidazolium, EMIM = 1-ethyl-3-methylimidazolium, TFSI = bis(trifluoromethanesulfonyl)imide, NEt_4 = tetraethylammonium, BF_4 = tetrafluoroborate, PIP_{13} = N-methyl-N-propylpiperidinium, FSI = bis(fluorosulfonyl)imide, PYR_{14} = *N*-butyl-*N*-methylpyrrolidinium PEGDA = poly(ethylene glycol) diacrylate, PVA = poly(vinyl alcohol), TMOS = Tetramethyl orthosilicate, PC = propylene carbonate, ACN = acetonitrile, [i] = max of the instantaneous power, [ii] = maximum power

TABLE 3 ELECTROCHEMICAL PERFORMANCE OF MICRO-SUPERCAPACITORS BASED ON 3D TOPOLOGY

REF	Electrode configuration	Electrode material[a]		3D scaffold		Electrode capacitance*	Areal power density	Device topology	Electrolyte[b] / Cell voltage (V)
		Deposition technique	Thickness (µm)	Materials / shape (fabrication technique)	Depth (µm)	($mF.cm^{-2}$)	($mW.cm^{-2}$)		
91	3D	MnO_2 (ED)	0.015	Nanoporous gold sputtered $Au_{0.25}Ag_{0.75}$ thin film then desalloying	0.75	1	0.45[i]	Interdigitated	1 M Na_2SO_4
94	3D	PANI (ED)	0.022	Nanoporous gold sputtered $Au_{0.25}Ag_{0.75}$ thin film then desalloying	0.1	3.8	0.41[i]	Parallel plate	PVA / H_2SO_4 / 0.8 V
43	3D	MnO2 (ED)	-	Si nanowires (CVD)	50	26	0.05[i]	Parallel plate	$LiClO_4$ doped PMPyrr-BTA Ionic Liquid / 2.2 V
176	3D	Ppy (ED)	0.1	Si nanotrees (CVD)	50	28	0.8[i]	Parallel plate	PYR_{13} - TFSI Ionic Liquid / 1.5 V
92	3D	MnO_2 (ED) and AC	0.1	Ni nanocones array (ED)	2	31.6	2[i]	Parallel plate	Ionogel (EMIM - BF_4 / Fused Silica) / 2.5 V
95	3D	Ppy (ED)	2	C-MEMS (SU8 photoresist pyrolysis)	140	200	1.6[i]	Interdigitated	1 M KCl
96	3D	PANI nanofiber (ED)	7	Microcavity on parylene polymer	15	260	3[i]	Interdigitated	PVA H_2SO_4 / 0.8 V
93	3D	RuO_2 (ED)	0.67	Pt nanotubes (Pt ED through AAO then AAO dissolution)	10 to 20	320	-	Single electrode	0.5 M H_2SO_4 / 1,3 V
26	3D	Carbon (CVD)	0.002	Si nanowires (chemical etching)	120	325	8[i]	Single electrode	EMIM - TFSI / 2.7 V
8	3D	MnO_2 (ED)	0.35	Si micro-tubes (Plasma etching)	68	452	20[i]	Interdigitated	0.5 M Na_2SO_4 / 0.8 V
84	3D	MnO_2 (ED)	0.3	Si micro-tubes (Plasma etching)	55	670	-	Single electrode	0.5 M Na_2SO_4 / 0.8 V
177	3D	RuO_2 (ED)	-	Carbon nanowall (CVD)	12	1 094	31.3[ii]	Parallel plate	PVA / H_3PO_4 / SiWa / 0.9 V
9	3D	Graphene LSG and MnO_2 (ED)	1	3D LSG	15	1 536	1	Interdigitated	1 M Na_2SO_4 / 0.9 V
12	3D	RuO_2 (ED)	-	Macroporous gold thick film (ED)	80	3 473	7.9[i]	Parallel plate	PVA / H_3PO_4 / SiWa / 0.9 V

[a] LSG = Laser-scribed Graphene, CVD = chemical vapour deposition, ED = electrodeposition, PANI = polyaniline, PPy = Polypyrrole, * If not mention, estimated from $C_{electrode}$ = 4 x C_{MSC} for interdigitated topology and $C_{electrode}$ = 2 x C_{MSC} for parallel plate configuration, [b] EMIM = 1-ethyl-3-methylimidazolium, TFSI = bis(trifluoromethanesulfonyl)imide, BF4 = tetrafluoroborate, PYR13 = N-methyl-N-propyl pyrrolidinium, PMPyrr = 1-Methyl-1-propylpyrrolidinium, BTA = bis(trifluromethylsulfonyl)imide, SiWA = silicotungstic acid, PVA = poly(vinyl alcohol) , [i] = max of the instantaneous power, [ii] = maximum power